Applicability of machine learning-based downscaling method to climate change prediction

Takao Yoshikane[1,2]*, Kei Yoshimura[2]¶

[1]Precision Earth Ltd, Shibuya-ku, Tokyo, Japan

[2]Institute of Industrial Science, The University of Tokyo, Kashiwanoha, Kashiwa-shi, Chiba, Japan

*Corresponding author

E-mail takao-y@iis.u-tokyo.ac.jp

¶ The authors contributed equally to this work.

Abstract

The precipitation characteristics that cause water-related disasters strongly depend on local factors such as topography. Therefore, high-resolution climate change projection data is needed to accurately assess regional flood disaster risk. Climate models generally have low resolution and are insufficient to reproduce observed precipitation distributions. Downscaling techniques are usually applied to estimate detailed precipitation distributions. In recent years, machine learning techniques have been widely adopted for downscaling to improve accuracy. However, data-driven machine learning methods have been criticized for issues such as an inability to make appropriate extrapolations when predicting climate change, and there are currently very few examples of their application in this context. In this study, a machine learning–based downscaling bias correction method that recognizes hourly weather patterns in past and future climates was applied and its validity was examined. This method enables temporal and spatial downscaling and bias correction of multiple variables related to hydrological processes, while adequately reproducing climate change characteristics in climate models that are difficult to achieve using conventional methods. Although each variable was estimated independently, the temporal changes were highly correlated with reanalysis values, indicating that the variables were interrelated. Therefore, this simple method of

recognizing temporal and spatial distribution patterns can also be applied to hydrologically relevant climate model output variables, allowing downscaling and bias correction while accurately reflecting the climate change characteristics predicted by global climate models.

Introduction

Regional climatic characteristics are highly dependent on local topographic features. Therefore, high-resolution data are required to predict regional water resources and water-related disaster risks in detail [1, 2]. However, global climate models are computationally intensive. Therefore, global climate simulations usually need to be performed at coarse spatial resolutions [3]. Dynamic and statistical downscaling techniques have been used to obtain high-resolution climate prediction data [4, 5]. Dynamic downscaling typically uses high-resolution regional climate models, which require significant computational resources for long-term climate simulations. Errors in climate models are likely to be preserved or amplified by high-resolution regional climate models [6]. Climate change projections show substantial differences in climate change characteristics between global and regional climate models [7–9]. Statistical downscaling does not require large computational resources but cannot accurately reflect the effects of local topography; in some cases, the resulting characteristics may differ significantly from observations [10]. In recent years, many downscaling methods using machine learning have been developed to improve accuracy [11–14]. However, there are few cases in which machine learning techniques have been applied to climate change projections. Machine learning models are data-driven and may not accurately extrapolate beyond the range of the training data [15, 16]. To address this issue, a method was developed that incorporates physical constraints into machine learning models to improve predictive accuracy [17]. The methodology employed climate-invariant mapping to improve data efficiency, performance, and reproducibility across different climates. However, not all variables are necessarily applicable, and it is necessary to find a “feature transformation” that result in climate invariance and to verify its performance [17]. Another approach that has been applied to climate change projections is a machine learning–based downscaling method using hourly spatial distribution data, which exploits the strong relationship between the spatial distribution characteristics of precipitation over large areas and local precipitation characteristics [18]. This method estimates the characteristics of climate change by utilizing various weather patterns that emerge as a result of natural climate variability. Here, it is assumed that weather patterns will not change considerably from the past to the future.

For example, cold (warm) weather patterns observed during the training period are expected to appear more frequently in cold (warm) climates. If this assumption is incorrect, there will be a large discrepancy between the simulation results of the climate model and the climate change characteristics estimated using machine learning. This method can apply the trained patterns to various climate models by imposing a constraint requiring reproducibility of the physical model, that is, the ability to reproduce phenomena at fivefold or higher resolution. In this study, this method was further developed and downscaling experiments were conducted for past and future climates. Eight variables (precipitation, temperature, specific humidity, surface pressure, surface wind, and downward short- and longwave radiation) were used as inputs to land surface models for water-related risk assessment to verify whether extrapolation could be performed appropriately.

Materials and Methods

Overview of the machine learning method

A downscaling and bias correction method using machine learning [18] (hereafter referred to as YY2023) was developed to enable the application of climate model outputs, such as those from the World Climate Research Programme (WCRP) Coupled

Model Intercomparison Project Phase 6 (CMIP6). Numerical models can generally reproduce meteorological phenomena at a resolution approximately five times the grid size [19, 20]. Therefore, weather forecasts can reproduce weather events such as warm and cold fronts associated with low-pressure systems, as well as the time-varying characteristics of weather patterns within a domain. However, model biases owing to imperfections in numerical models, such as insufficient resolution, are inevitable [10, 21, 22]. Machine learning methods are expected to capture a close relationship between the simulated spatial distribution and observed values located at the center of the domain through weather patterns. It is assumed that climate models with similar resolutions reproduce weather systems with similar characteristics. Therefore, pattern recognition of the relationship between the spatial distribution of various factors simulated by weather forecast models and observational data is applicable to other models. In this study, the effectiveness of this method was demonstrated by applying pattern recognition to 20th Century Reanalysis Data (20CR) [23] and outputs from CMIP6 MIROC (MIROC) simulations [24]. This approach is expected to improve the accuracy of estimating the water-related disaster risks and water resources associated with climate change. In this study, the machine learning downscaling bias correction method was applied to estimate precipitation, temperature at 2 m, near-surface wind at 10 m, specific humidity, surface pressure, and downward short- and longwave radiation over land areas worldwide, excluding regions north of 84°N and south of 60°S (Fig 1), and the applicability of the method was demonstrated to climate models. We set 7 × 7 grid points as the explanatory variables (1.5° grid spacing) and divided the center grid of the explanatory variables into a 3 × 3 grid to define the objective variables (1.5° grid spacing) (Figs. 1b and 2). In this method, temporal downscaling was simultaneously performed from 3-h values to 1-h values (Figs. 2 and 3 and Table 1). Machine learning effectively corrects the spatial distribution of each variable. The estimated values of each variable reproduce the time-varying characteristics well but tend to be slightly underestimated. Therefore, after machine learning, the quantile mapping (QM) method was applied to the estimated values to perform quantitative correction [18], except for downward shortwave radiation (Fig. 4). Regarding shortwave radiation, no significant need for quantitative correction is determined because the range of values is not expected to change in the future climate. Quantitative bias in global climate model simulations is small, and sufficient accuracy can be achieved through downscaling and bias correction using the machine learning method alone. In addition, an experiment was performed in which only the QM method was applied to evaluate differences relative to this method. In the training process, data upscaled to 0.5° and 1.5° using ECMWF

Reanalysis v5 (ERA5) [25] were used as objective and explanatory variables, respectively. The learning period was 11 years, from 2008 to 2018, and a classifier was created for each month (Table 1). For downscaling from 3-h values to 1-h values, data from 3 h before and after the target period were used as explanatory variables, and an hourly classifier was created for each period (Fig 3). For inference, the 20CR and MIROC data were upscaled to 1.5° and applied to the classifier created during the learning process. Finally, the 20CR data and MIROC output values were downscaled to a spatial resolution of 0.5° and a temporal resolution of 1 h (Table 1).

Fig 1. Calculation domain and the domains of explanatory variables and objective variables used in machine learning. (A) The calculation domain (gray area) is the land area from 60°S to 84°N. B) The thick frame defines the explanatory variables (1.5° grid spacing) on a 7 x 7 grid, and the thin inner frame is divided into a 3 x 3 grid to define the objective variables (0.5° grid spacing).

Fig 2. Schematic view of the training and inference processes. The numbers of explanatory and response variables (dimensions) were 147 and 1, respectively. A 7 × 7 grid was selected as the explanatory variable, including data from 3 h before ("−3h") and 3 h after (“+3h”) the target time (1.5° grid spacing). The central grid of the explanatory variables was divided into 3 × 3 grid points, which were selected as the objective variables (0.5° grid spacing). Twenty-seven classifiers were created for each grid with a coarse mesh (spatial downscaling) and for temporal downscaling from three-hourly to hourly resolution. For variables other than precipitation and downward short- and longwave radiation, “0 h,” “+1 h,” and “+2 h” represent the initial time, 1 h later, and 2 h later, respectively. Precipitation and solar radiation corresponded to averages over 0–1 h, 1–2 h, and 2–3 h.

Fig 3. Schematic view of temporal downscaling. The explanatory variables used are data from three hours before and after the “target time.” Precipitation and downward short- and longwave radiation were estimated using 3-h averages, whereas the other variables were estimated using snapshot values. At the target time, the objective variable is set for each hour. “Initial time,” “1st time,” “2nd time,” and “3rd time” represent 0 h, 1 h, 2 h, and 3 h after the initial time in the target time period. “Initial time,” “1st time,” and “2nd time” are used for variables other than precipitation and downward short- and longwave radiation and correspond to “0h,” “+1h,” and “+2h” in

Fig. 2. Precipitation and downward short- and longwave radiation correspond to three-hourly integrated or average values for 0–1 h, 1–2 h, and 2–3 h.

Table 1. Experimental conditions.

Experiment	MLDS_20CR	MLDS_MIROC
Explanatory variable	ERA5 reanalysis data (upscaled 1.5degree) 7 by 7 grids	Same as MLDS_20CR
Objective variable	ERA5 reanalysis data (upscaled 0.5 degree)	Same as MLDS_20CR
Training term	Every month from 2008 to 2018	Same as MLDS_20CR
Target mode output	NOAA-CIRES-DOE 20th Century Reanalysis V3	Atmosphere and Ocean Research Institute; Centre for Climate System Research - National Institute for Environmental Studies: WCRP CMIP6: the MIROC team MIROC6 model output.
Downscaling term	Past: Every month from 1955 to 1984	Historical: Every month from 1985 to 2014
	Present: Every month from 1985 to 2014	SSP126: Every month from 2071 to 2100

Fig 4. Flowchart of the method. DSWR denotes downward shortwave radiation.

Bias correction and downscaling methods using machine learning.

A support vector machine regression (SVM–SVR) [26], constructed in a previous study [18], was used. An SVM is a supervised learning technique that uses a subset of the data to derive predictions from support vectors. An SVM seeks to obtain optimal results by finding a maximum-margin hyperplane determined by maximizing the distance between support vectors. Compared with other machine learning techniques, such as neural networks and random forests, SVM has several advantages [27–29]. For example, SVR has been shown to perform well, even with small sample sizes [26]. SVMs have been employed in various fields, including meteorology, hydrology, disaster prevention management, and water resources management, and have proven effective in recognizing rare precipitation events [30–32]. In this study, the SVM library was used in the Intel® Extension for Scikit-learn (ver. 2023.1.1) [33] and the Epsilon-Support Vector Regression (SVR) implementation in Scikit-learn (ver. 1.2.2) [34]. The SVR method requires the hyperparameters gamma, C, and epsilon to be specified. Gamma is a kernel parameter that specifies the width of the Gaussian radial basis function (RBF) kernel, C is the penalty constraint error, and epsilon is the width of the dead zone [35]. Determining these hyperparameters is crucial for improving the generalizability of precipitation estimates. However, determining the optimal parameters requires substantial computational resources [34, 35]. Therefore, it is necessary to efficiently obtain optimal hyperparameters. Although hyperparameters can be specified at each time point in this method, this approach is highly inefficient because determining the optimal values over the entire domain requires substantial computational resources. Therefore, the same set hyperparameter values were applied to all the grid cells in the domain, following the same methodology used in previous studies involving YY2023 (S1 Table) [18, 36].

SVR method.

The SVR method requires the hyperparameters gamma, C, and epsilon to be set. Gamma is the kernel function parameter that specifies the width of the Gaussian radial basis function kernel, C is the penalty constraint error, and epsilon is the width of the dead zone [35].

In the SVM method, the vector $x=(x_1,x_2,x_3........,x_p)^T$ consisting of p explanatory variables is the input, and a classifier is trained to correctly output the objective variable $f(x_i)$. By introducing the intercept b and the coefficient vector $w=(w_1,w_1,w_1.......,w_p)^T$, the linear regression function was defined as follows:

$$f(x_i)=w^T x_i+b \quad (1)$$

In this function, b and w are estimated to satisfy this relationship. In SVR, the non-negative parameter ε is set in advance, and only large residuals of e_i that exceed the range of $-\varepsilon \le e_i \le \varepsilon$ are recorded as penalties of ξ_i. The parameters are estimated to minimize the following equation:

$$\psi_\varepsilon(w,\xi) = \frac{1}{2}\|w\|_2^2 + C\sum_{i=1}^{n}\xi_i \quad (2)$$

$$\| w \|_2 = \sqrt{w_1^2 + w_1^2 + \cdots + w_p^2} \quad (3)$$

However, the following restrictions apply.

$$-\varepsilon - \xi_i \leq f(x_i) - (w^T x_i + b) \leq \varepsilon + \xi_i \quad (4)$$

In the above equations, C is the penalizing constraint error and, ε (epsilon) is the width of the insensitive zone. To determine the nonlinear regression equation, a feature map *φ(x)* that represents the vector of the nonlinear terms (features) of the explanatory variables was introduced. The regression function using the feature map is as follows:

$$f(x) = w^T \phi(x) + b \quad (5)$$

To avoid increased computational cost owing to increasing dimensionality of the feature space, kernel functions that can express the inner products in the feature space were introduced.

$$k(x_1, x_2) = \phi(x_1)^T \phi(x_2) \quad (6)$$

The inner product of two vectors is maximized when they have the same direction. Therefore, the kernel function can be interpreted as the similarity between two vectors in the feature space. However, when the dimensions of the feature space are large, calculating the inner product (6) is difficult. Therefore, the kernel method uses the following function, which is the inner product in a high-dimensional space:

$$k(x_1, x_2) = \exp(-\gamma \| x_1 - x_2 \|^2) \quad (7)$$

This function is called the Gaussian radial basis function kernel and, γ (gamma) is the kernel function parameter [37,38]. The hyper-parameters and scale factors for each variable are shown in S1 Table.

Training and test data.

The fifth-generation ECMWF reanalysis for global climate and weather (ERA5) hourly data were used as the training data for 11 years, from 2008 to 2018. As test data, the 20th century reanalysis data (20CR) for 60 years, from 1955 to 2014, and climate model data (MIROC) for historical data from 1985 to 2014 and future projections for the SSP126 scenario from 2071 to 2100 were used. The resolution of the 20CR and MIROC data was adjusted to 1.5° for consistency with the recognition patterns produced by the ERA5 reanalysis data. The variables were estimated at a resolution of 0.5° by downscaling them to a fine grid (3 × 3) using the same hyperparameters and feature ranges (7 × 7 grid points) used in the recognition pattern of the weather forecast model (Figs 1, 2, and 3; Table 1).

Quantile mapping method

To perform quantitative corrections, the CDF transformation method [39] was applied to the machine learning downscaling estimates, except for downward shortwave radiation. In machine learning methods, the accuracy is highly dependent on the number of samples. Heavy rainfall results in a small number of samples, which makes it difficult to accurately estimate rainfall. Techniques such as undersampling and oversampling are available to correct for unbalanced sampling [40]. In this study, the quantile mapping method (CDFt in the R package) [41] was used instead of undersampling or oversampling, considering the complexity of the adjustment. "CDF-t" assumes that there exists a transformation T that can convert the CDFs of GCM variables (e.g., temperature, precipitation, wind speed) into CDFs representing long-term variables at a local scale. To estimate the quantitative correction for future outputs of machine learning estimates, the transformation T is:

$$T(F_{Gh}(x)) = F_{Oh}(x) \quad (8)$$

$$T(F_{Gf}(x)) = F_{Of}(x) \quad (9)$$

where F_{Oh} is the CDF of observation data over current period, and F_{Gh} is the CDF of the bilinearly interpolated simulation data over current period. F_{Of} and F_{Gf} are the equivalent CDFs of F_{Oh} and F_{Gh}, respectively, for future (or simply different) periods. To model T,

x in *Gh* in Equation (1) with *F(u)*, where u is [0,1] and the following relationship is obtained:

$$T(u) = F_{Oh} \circ F_{Gh}^{-1}(u) \quad (10)$$

Hence, assuming that the relationship (4) remains valid, the CDF is provided by

$$F_{Of}(x) = T(F_{Gf}(x)) = F_{Oh} \circ F_{Gh}^{-1}(u) \circ F_{Gf}(x) \quad (11)$$

In the CDFt package, Eq. (1) reconstructs F_{Of} from F_{Oh}, F_{Gh}, and F_{Gf}, and Eq. (8) performs quantile mapping from F_{Of} and F_{Gf} to correct G_f. In practice, F_{Oh}, F_{Gh}, and $\mathrm{F_{Gf}}$ were estimated using the empirical cumulative distribution function. However, the CDFt method only works correctly when the observed values of *Oh* and *Gh* have similar ranges. In this study, we used ERA5 data with 0.5° resolution from 2008 to 2018 and 20CR and MIROC data over the current period from 1985 to 2014 instead of *Oh* and *Gh*. Instead of *Gf*, the machine learning estimates use 20CR for past period from 1955 to 1984 and MIROC for future projection from 2071 to 2100 (Fig 5).

Fig 5. Schematic view of quantile mapping method. F_{Oh} is observation (ERA5 reanalysis data) at 0.5°. F_{Gh} and F_{Gf} are present and future/past climate model outputs (20CR and MIROC, respectivery). F_{Of} is quantitatively corrected value (final product).

Results

Validation of the downscaling bias correction method

July is the month with an active Asian monsoon that brings large amounts of rainfall. This not only causes frequent flooding and other water disasters but also has a major impact on water resources; therefore, estimating the amount of rainfall during this period is extremely important. Figs 6 and 7 show the precipitation and temperature distributions for July over the global and Asian monsoon regions for the 30-year average values of 20CR, MLDS_20CR, and ERA5 from 1955 to 1984. Downscaling the 20CR data using this method confirmed that the distribution of precipitation and temperature were almost identical to that of ERA5. The precipitation characteristics corresponding to the topography were reproduced, indicating that the downscaling and bias correction methods were effective. The detailed spatial distribution characteristics of the temperature distribution corresponding to the topography were also estimated. Correction of the temperature distribution in alpine zones has a large effect on snow accumulation and snowmelt; therefore, it is also important for estimating water resources. The correlation coefficients and RMSEs of the spatial distributions of the eight variables in the 30-year average values of MLDS_20CR, 20CR, and ERA5 showed that, relative to ERA5, the bias of 20CR bias was significantly improved in MLDS_20CR for all variables (Fig 8). In particular, the overestimation of 20CR in the low-temperature range was improved by MLDS_20CR, indicating that the bias was corrected and the performance was improved by this method. The spatial distribution characteristics of spatial distributions were accurately well estimated using by this method (S1, S2, and S3 Figs).

Fig 6. Precipitation distribution characteristics in July. Thirty-year average of precipitation in July from 1955 to 1984 in the global and Asian monsoon area of 20CR, MLDS_20CR, and ERA5, respectively. (A) Global area of 20CR. (B) Global area of MLDS-20CR. (C) Global area of ERA5. (D) Asian monsoon area of 20CR. (E) Asian monsoon area of MLDS-20CR. (F) Asian monsoon area of ERA5.

Fig 7. The same figure as Fig 6 except for temperatures.

Fig 8. Bias correction effect using this method. Scatter diagrams of the 30-year average of annual mean values of MLDS_20CR for 20CR and ERA5 for the first 30 years, from 1955 to 1984. (A) 20CR in temperature (TEMP2M). (B) 20CR for downward long-wave radiation (DLWR). (C) 20CR at specific humidity (SHUM). (D) 20CR for downward short-wave radiation (DSWR). (E) ERA5 as a function of temperature (TEMP2M). (F) ERA5 under downward long-wave radiation (DLWR). (G) ERA5 at specific humidity (SHUM). (H) ERA5 under downward short-wave radiation (DSWR). (I) 20CR surface pressure (SP). (J) 20CR in the near surface winds (zonal) at 10m (U10M). (K) 20CR under near-surface winds (meridional) at 10m (V10M). (L) 20CR during precipitation (PREC). (M) ERA5 surface pressure (SP). (N) ERA5 under near-surface winds (zonal) at 10m (U10M). (O) ERA5 under near-surface winds (meridional) at 10m (V10M). (P) ERA5 during precipitation (PREC). MLDS_20CR and ERA5 were upscaled to match the resolution of 20CR. The correlation coefficients (R) and RMSEs of the spatial distributions are shown in each diagram.

The 99th percentile values of the hourly data except for precipitation and temperature in the first 30 years, and the climatic different values between the first and last 30 years in ERA5 and MLDS_20CR are shown in S4 and S5 Figs. The spatial distribution characteristics of extreme values in MLDS_20CR corresponded well with those in ERA5, with a high correlation of >0.97. The values of precipitation and temperature data are described in detail in the following subsections.

Validation for past climate change

The spatial distribution of the annual mean climate change for the eight variables of 20CR, MLDS_20CR, and ERA5 over the first 30 years (1955–1985) versus the second 30 years (1985–2014) is shown in Fig 9 and S6 and S7 Figs. The shaded areas indicate areas with a significant change at the 95% significance level with respect to interannual variation. For the seven variables, including temperature (TEMP2M), except for precipitation (PREC), the climate change distribution of MLDS_20CR was almost the same as that of 20CR, and the change characteristics were consistent with ERA5. The DSWR of MLDS_20CR also closely reproduced the change characteristics of the 20CR, even though no quantitative correction was performed (Figs 9G and 9H). The areas showing significant changes corresponded well. Regarding precipitation, the amount of climate change was small, and the spatial distribution characteristics of the amount of change were different. The correlation coefficients and RMSEs of MLDS_20CR and 20CR for the annual mean climate change of the eight variables also showed that, except for precipitation, the correlation coefficients were over 0.93, and the quantitative correspondence was almost the same. However, for precipitation, the correlation was weak, and the quantitative correspondence was not consistent (Fig 10).

However, the spatial distribution of climate change trends in ERA5 corresponded well with those in MLDS-20CR and 20CR, but the amount of change at each grid point did not correspond well (S8 Fig). This indicates that the climate change at each grid point is small and that the climate differences between different reanalysis data do not match well. The frequency and extreme values of precipitation and temperature are important for assessing flood disaster risk in a region. The performance of the temporal downscaling from three-hourly to hourly was confirmed by examining the frequency of hourly precipitation. Fig 11 shows the annual frequency of hourly precipitation events with precipitation of 1 mm or more in the first 30 years, and the climate difference values between the first and second 30 years in ERA5 and MLDS_20CR. Regarding the spatial distribution of frequency over the first 30 years, MLDS_20CR estimated the same regional distribution characteristics as ERA5, and although there was a tendency for it to be slightly underestimated in the tropical regions of Africa, it showed a high correlation of 0.98. However, the correlation coefficient for climate change with ERA5 was 0.30, which is a small correlation, and the amount of change by region did not match. The 99th percentile values of 1-hour precipitation (shaded areas indicate areas where the change in interannual variability is significant at the 95% confidence interval) are shown in Fig 12. In the spatial distribution of the first 30 years, the distribution characteristics of heavy rainfall were well estimated, and the correlation with ERA5 (0.92) was also high. In contrast, the correlation coefficient of climate change with ERA5 was 0.03, indicating there was almost no correlation, and the amount of change did not match. The frequency of temperatures below 0 °C has a substantial impact on water resources through snow accumulation and melting. Fig 13 shows the spatial distribution of the frequency of hourly temperatures below 0 °C (throughout the year). For the spatial distribution of the frequency over the first 30 years, MLDS_20CR estimated nearly the same regional distribution characteristics as ERA5 and showed a high correlation (0.99) with ERA5. However, its correlation with climate change was relatively low (0.73). The extent of climate change varies greatly in some regions, particularly in the coastal areas of the Arctic and alpine regions. Fig 14 shows the 99th percentile values of the hourly temperatures in the first 30 years, and the climate differences between the first and last 30 years in ERA5 and MLDS_20CR. MLDS_20CR estimated nearly the same regional distribution characteristics as ERA5 and showed a high correlation (0.99) with ERA5. In contrast, climate change has a low correlation with ERA5 (correlation coefficient = 0.36).

Fig 9. Estimation of climate change characteristics using 20CR. Annual mean climate difference between the first 30 years (past) and the last 30 years (present). (A) 20CR in precipitation (PREC). (B) MLDS-20CR in precipitation (PREC). (C) ERA5 in precipitation (PREC). (D) 20CR in temperature (TEMP2M). (E) MLDS-20CR at temperature (TEMP2M). (F) ERA5 at temperature (TEMP2M). (G) 20CR for downward short-wave radiation (DSWR). (H) MLDS-20CR for downward short-wave radiation (DSWR). (I) ERA5 for downward short-wave radiation (DSWR). Shaded areas indicate significant increases with 95% confidence intervals using Welch's t-test.

Fig 10. Relationship between climate change simulated by the climate model and the values estimated by this method. Scatter diagrams of annual mean climate difference values between the first 30 years (past) and the last 30 years (present) of MLDS_20CR for 20CR. (A) Temperature (TEMP2M). (B) Downward long-wave radiation (DLWR). (C) Specific humidity (SHUM). (D) Downward short-wave radiation (DSWR). (E) Surface pressure (SP). (F) Near-surface winds (zonal) at 10 m (U10M). (G) Near-surface winds (meridional) at 10 m (V10M). (H) Precipitation (PREC). MLDS_20CR was upscaled to match the resolution of 20CR.

Fig 11. Annual frequency of hourly precipitation events with precipitation of 1 mm or more in the first 30 years, and the climate difference values between the first and last 30 years in ERA5 and MLDS_20CR. (A) The frequency in ERA5. (B) The frequency of MLDS_20CR. (C) Frequency scatter diagram for ERA5 and MLDS_20CR. (D) The climate difference values in ERA5. (E) Climate difference values in MLDS_20CR. F) The scatter diagram of climate different values in ERA5 and MLDS_20CR.

Fig 12. The 99th percentile values of hourly precipitation in the first 30 years, and the climate difference values between the first and last 30 years in ERA5 and MLDS_20CR. (A) The 99th percentile values in ERA5. (B) The 99th percentile values in MLDS_20CR. (C) Scatter diagram of the 99th percentile values of ERA5 and MLDS_20CR. (D) The climate difference values in ERA5. (E) Climate difference values in MLDS_20CR. (F) Scatter diagram of the climate difference values in ERA5 and MLDS_20CR. Shaded areas indicate areas where the change in interannual variability was significant at the 95% confidence interval.

Fig 13. The spatial distribution of the annual frequency of hourly temperatures below 0 °C in the first 30 years, and the climate difference values between the first and last 30 years in ERA5 and MLDS_20CR. (A) The frequency in ERA5. (B) The frequency of MLDS_20CR. (C) Frequency scatter diagram for ERA5 and MLDS_20CR. (D) The climate difference values in ERA5. (E) The climate difference values in MLDS_20CR. (F) Scatter diagram of the climate difference values in ERA5 and MLDS_20CR. Shaded areas indicate areas where the change in interannual variability is significant at the 95% confidence interval.

Fig 14. The 99th percentile values of hourly temperatures in the first 30 years, and the climate difference values between the first and last 30 years in ERA5 and MLDS_20CR. (A) The 99th percentile values in ERA5. (B) The 99th percentile values in MLDS_20CR. (C) Scatter diagram of the 99th percentile values of ERA5 and MLDS_20CR. (D) The climate difference values in ERA5. (E) Climate difference values in MLDS_20CR. (F) Scatter diagram of climate different values in ERA5 and MLDS_20CR. Shaded areas indicate areas where the change in interannual variability is significant at the 95% confidence interval.

Applicability to future climate change predictions

SSP126 is one of the most optimistic global warmings scenarios and predicts that the rise in temperature from pre-industrial levels will be limited to approximately 1.5-1.7 °C. Without the ability to properly extrapolate future projections, even for scenarios with small temperature increases, it would be to apply this method to future climate change scenarios. In this study, a scenario with a relatively gradual increase in temperature was selected and verified whether it was applicable to future projections. The characteristics of the spatial distributions of the 30-year mean from 1985 to 2014 in the MLDS_MIROC historical data corresponded well with ERA5 and corrected the biases in the MIROC historical data (S9, S10, and S11 Figs). The spatial distributions of climate change for the eight variables in MIROC and MLDS_MIROC historical (1985–2014) and SSP126 (2071–2100) are shown in Fig 15 and S12 and S13 Figs. Except for precipitation, MLDS_MIROC quantitatively corresponded well with the changes in MIROC, with correlation coefficients greater than 0.89. For precipitation, the correlation coefficient was somewhat high at 0.58; however, the amount of change was generally small, and the areas where significant changes occurred were sparse.

Fig 15. Relationship between climate change predicted by the climate model and the values estimated by this method. Annual mean climate difference between the present 30 y (historical scenario) from 1985 to 2014 and the future 30 y (SSP126 scenario) from 2071 to 2100. (A) MIROC for precipitation (PREC). (B) MLDS_MIROC for PREC. (C) Scatter diagram of PREC in MIROC and MLDS_MIROC, (D) MIROC for temperature (TEMP2M). (E) MLDS_MIROC for TEMP2M. (F) Scatter diagram of TEMP2M in MIROC and MLDS_MIROC, (G) MIROC for downward shortwave radiation (DSWR). (H) MLDS_MIROC for DSWR. (I) Scatter diagram of DSWR in MIROC and MLDS_MIROC. Shaded areas indicate significant increases with 95% confidence intervals using Welch's t-test. MLDS_MIROC was upscaled to match the resolution of MIROC.

Correspondence of estimated values of each variable to weather events

In this method, each variable is estimated using different explanatory and objective variables. Therefore, it was necessary to investigate whether a relationship exists between these variables over time. Fig. 16 shows the time series of the eight variables in 20CR, MLDS_20CR, and ERA5 for a specific location in July 1985. In

Japan, July is the month when the rainy season changes to a dry period, and changes in the climatic characteristics of the eight variables are also noticeable. For time changes other than precipitation, a high correlation (> 0.74) is shown with ERA5. Each element changed in response to the difference between the rainy and dry periods and was consistent with the weather patterns. In 20CR, the effects of terrain (altitude) due to low resolution can be observed (especially in pressure); however, this is corrected by this downscaling method, and the data become closer to ERA5. The correlation between precipitation and ERA5 is low (0.37). Slight differences in the location and timing of the disturbance passage were observed between ERA5 and 20CR, causing large local differences in the temporal variation of precipitation.

Fig 16. Temporal variations at a specific point (136E, 36N) in July 1985. (A) Precipitation (PREC). (B) Temperature (TEMP2M). (C) Specific humidity (SHUM). (D) Near-surface wind at 10 m (zonal) (U10M). (E) Surface pressure (SP). (F) Near-surface wind at 10 m (meridional) (V10M). (G) Downward longwave radiation (DLWR). (H) Downward shortwave radiation (DSWR). R is the correlation coefficient between MLDS_20CR and ERA5.

Comparison with quantile mapping method

Quantile mapping is a commonly used downscaling technique. In general, this strongly depends on the characteristics of the model output data. Therefore, if the meteorological characteristics at the downscaled grid points differ significantly between the observations and the model output, the QM estimates may differ significantly from the observations. Applying QM alone does not adequately correct bias in the spatial distribution of precipitation [38]. S14 Fig shows the temporal variation in temperature in July 1985 for QM only, ERA5, 20CR, and MLDS_20CR at a specific grid point. While MLDS_20CR had almost the same temporal variation characteristics as ERA5, the reproducibility of diurnal variation decreased in QM, and the variation characteristics were closer to those of 20CR than to ERA5. MLDS_20CR is an hourly estimate, whereas QM is a three-hourly estimate, therefore, the reproducibility of daily changes is inevitably low. Furthermore, if the proportion of the ocean area is large at the model grid point, the diurnal variation in the QM estimate may be smaller owing to its influence. In contrast, MLDS_20CR can estimate variation characteristics that reflect local influences, such as diurnal variation.

Discussion

To investigate the applicability of this method to climate change, downscaling and bias correction of eight climate model variables (precipitation, temperature, surface pressure, surface wind, specific humidity, downward shortwave radiation, and longwave radiation) used as inputs to a hydrological model was performed. The estimates had almost the same spatial distribution characteristics as the ERA5 reanalysis. This indicates that the weather pattern characteristics of each variable simulated by the climate model are consistent with the ERA5 reanalysis and that the classifier trained using the ERA5 reanalysis can be applied to climate model output. If the climate model has a bias in large-scale circulation (e.g., a large north–south shift in the storm track), it may cause a large error in precipitation frequency in the region, which may have a considerable impact on the precipitation amount. These biases in climate models also affect precipitation characteristics estimated using this method, leading to large discrepancies between estimates and observations. Therefore, this method is applicable only if the large-scale circulation characteristics reproduced by climate models do not deviate significantly from observations. This method reproduced the hourly frequency and extreme value distribution of precipitation, indicating that precipitation events were effectively downscaled in space and time. This method can also reproduce the spatial distribution of the frequency of temperatures below 0°C, except in special cases, making it useful for evaluating water resources such as snow accumulation and snowmelt. To reproduce past climate changes, the method reproduced the same climate change patterns as the reanalysis values and climate models, except for precipitation. This indicates that various hourly spatial patterns during the current cold and warm seasons also apply to past weather patterns. Compared to ERA5, the climate change characteristics were well reproduced over a wide area, but the amount of climate change at each grid point was not as consistent as expected (S6 Fig). This is likely because the extent of climate change was small, and the difference in the characteristics of the reanalysis data between 20CR and ERA5 was greater than the extent of climate change. The characteristics of the change in precipitation were unclear, and there were few areas where the change was statistically significant. This suggests that the natural variability of precipitation is greater than the influence of global warming and that the differences in the characteristics of the reanalysis data used for downscaling (20CR and ERA5), such as slight differences in storm tracks, significantly affect the distribution pattern of downscaled local precipitation. Climate change in some coastal and alpine regions of the Arctic has underestimated the frequency of subfreezing temperatures and the 99th percentile values. This was assumed to be due to changes in the local environment, such as the disappearance of glaciers. If the local environment changes significantly, it may be difficult to respond in certain cases. In the future, it will be necessary to incorporate the effects of glacier loss into our estimates. By linking machine learning estimates with hydrological models, it may be possible to adjust temperature to reflect the effects of glacier loss.

Projections of future climate estimated patterns of climate change are almost identical to those reproduced in the climate model, with the exception of precipitation. Precipitation was relatively more strongly correlated with future climate change than with past climate change. This may be due to clearer sensitivity to global warming. Regarding the so-called extrapolation issue, it is assumed that the extrapolation of this method works properly unless climatic characteristics change significantly, such as glacial disappearance. The correlation between the time variation of each variable and ERA5 was relatively high at 0.71 or more, except for precipitation, and the time variation characteristics corresponded well. On the other hand, with regard to precipitation, even small differences in storm tracks between ERA5 and 20CR can lead to large differences in the local temporal variability of precipitation due to the influence of topography. Therefore, it is necessary to estimate the impacts of natural variability and sensitivity to global warming on precipitation using ensemble experiments. In general, the meteorological variables reproduced by climate models are related through synoptic-scale weather patterns, and by applying this method to estimate the relationship between large-scale and local fields, the relationship between each variable was confirmed, even in downscaling estimations.

Several studies have applied machine learning methods to climate change projections [12, 15]. In addition to the extrapolation problem, it may be difficult to apply the patterns learned using weather forecast model outputs and reanalysis data to climate models. This method uses the characteristics of a numerical model that can reproduce phenomena five times or more the grid spacing as explanatory variables, making it relatively versatile and likely to be flexibly applied to any numerical forecast model or climate model. The fact that explanatory variables can be estimated with high accuracy, despite their simplicity, suggests a close relationship between explanatory and objective variables. The advantage of applying deep learning models instead of traditional machine learning models, such as support vector regression (SVR), may be very small because the method is strongly constrained by the simple relationship between the objective and explanatory variables.

Climate change downscaling experiments using regional models can sometimes reveal future climate change patterns that are quite different from those predicted by global climate models, making interpretation difficult [7–9]. This could be because high-resolution regional models can reproduce phenomena that are difficult to reproduce using low-resolution global climate models. However, it is also possible that the errors are simply amplified by regional climate models [6]. In contrast, this method can accurately reflect the climate change characteristics of global climate models and does not require consideration of the uncertainties that arise when applying regional models. Therefore, applying this method to highly developed global climate model simulations with greatly improved climate reproducibility will enable local future predictions with reduced model uncertainties and is expected to significantly improve the accuracy of water disaster predictions.

Conclusions

To investigate the extrapolation problem when applying machine learning to climate change projections, downscaling and bias correction was performed using 20th century reanalysis data and CMIP6 model data. This method has been demonstrated to enable highly accurate downscaling of atmospheric variables, except for precipitation, to regional details, while retaining the characteristics of climate change in global climate models. The climate change characteristics of precipitation differed from those of the climate model. This is presumably because the influence of natural variability is far greater than that of climate change, making it difficult to accurately reproduce the quantitative characteristics. Although each variable was estimated independently, it was highly correlated with the corresponding reanalysis values, indicating that the variables were interrelated through weather patterns. Therefore, this simple method can also be applied to hydrologically relevant climate model output variables, allowing downscaling and bias correction while accurately reflecting the climate change characteristics predicted by global climate models. On the other hand, the frequency of temperatures below 0 °C and the 99th percentile of temperature values were confirmed to be underestimated, indicating that this method alone has difficulty dealing with cases where temperature fluctuations become large due to extreme changes in regional characteristics, such as the disappearance of glaciers. In the future, this method is planned to be coupled with a hydrological model, improving its adaptability to extreme local characteristics.

Acknowledgments

The authors would like to thank ERA5, Integrated Research Program for Advancing Climate Models (TOUGOU Program) CMIP6 simulation data by Global Climate Model MIROC6: CMIP, NOAA-CIRES-DOE 20th Century Reanalysis V3 contains

objectively analyzed four-dimensional weather maps and their uncertainty from the early 19th century to the 21st century. (20CR Project).

Author Contributions

Conceptualization: Takao Yoshikane and Kei Yoshimura.

Formal analysis: Takao Yoshikane.

Methodology: Takao Yoshikane.

Project administration: Takao Yoshikane.

Supervision: Kei Yoshimura.

Visualization: Takao Yoshikane.

Writing the original draft: Takao Yoshikane.

Writing, review and editing: Takao Yoshikane and Kei Yoshimura.

References

1. Viviroli D, Weingartner R. The hydrological significance of mountains: from regional to global scale. Hydrol Earth Syst Sci. 2004; 8(6):1017–1030.
2. Payne E, Demory E, Leung LR, Ramos AM, Shields CA, et al. Responses and impact of atmospheric rivers on climate change. Nat Rev Earth Environ. 2020;

1(3):143–157.

3. Duffy PB, Govindasamy B, Iorio JP, Milovich J, Sperber KR, Taylor KE, et al. High-resolution simulations of the global climate. Part 1: Present climate. Clim Dyn. 2003; 21:371–390.
4. Tang J, Niu X, Wang S, Gao H, Wang X, Wu J. Statistical and dynamical downscaling of regional climate in China: present climate evaluations and future climate projections. J Geophys Res Atmos. 2016; 121(5):2110–2129.
5. Vrac M, Drobinski P, Merlo A, Herrmann M, Lavaysse C, Li L, et al. Dynamic and statistical downscaling of the French Mediterranean climate: uncertainty assessment. Nat Hazards Earth Syst Sci. 2012; 12(9):2769–2784.
6. Pielke RA, Wilby RL. Regional climate downscaling: what is the point? Eos Trans AGU. 2012; 93(5):52–53.
7. Katragkou E, Sobolowski SP, Teichmann C, Solmon F, Pavlidis V, Rechid D, et al. Delivering an improved framework for new-generation CMIP6-driven EURO-CORDEX regional climate simulations. Bull Am Meteorol Soc. 2024; 105(6):E962–E974.
8. Chen L. Uncertainties in solar radiation assessment in the United States using climate models. Clim Dyn. 2021; 56:665–678. doi:10.1007/s00382-020-05498-7.

9. Boé J, Somot S, Corre L, et al. Large discrepancies in summer climate change in Europe as projected by global and regional climate models: causes and consequences. Clim Dyn. 2020; 54:2981–3002. doi:10.1007/s00382-020-05153-1.

10. Maraun D, et al. Towards process-informed bias correction for climate change simulations. Nat Clim Change. 2017; 7:764–773.

11. Rampal N, Gibson PB, Sood A, Stuart S, Fauchereau NC, Brandolino C, et al. High-resolution downscaling with interpretable deep learning: rainfall extremes over New Zealand. Weather Clim Extremes. 2022; 38:100525.

12. Rampal N, Hobeichi S, Gibson PB, Baño-Medina J, Abramowitz G, Beucler T, et al. Enhancing regional climate downscaling through advances in machine learning. Artif Intell Earth Syst. 2024; 3(2):230066.

13. Wang F, Tian D. Deep-learning-based bias correction and downscaling of multiple climate model simulations. Clim Dyn. 2022; 59(11):3451–3468.

14. Buster G, Benton BN, Glaws A, King RN. High-resolution meteorology with climate change impacts from global climate model data using generative machine learning. Nat Energy. 2024; 9(7):894–906.

15. Eyring V, Collins WD, Gentine P, Barnes EA, Barreiro M, Beucler T, Zanna L. Pushing frontiers in climate modelling and analysis using machine learning. Nat

Clim Change. 2024; 14(9):916–928.

16. González-Abad J, Gutiérrez JM. Are deep-learning methods suitable for downscaling global climate projections? Review and inter-comparison of existing models. arXiv Preprint. 2024; arXiv:2411.05850.

17. Beucler T, et al. Climate-invariant machine learning. Sci Adv. 2024; 10(6):eadj7250.

18. Yoshikane T, Yoshimura K. Downscaling and bias correction methods for climate model ensemble simulations of local-scale hourly precipitation. Sci Rep. 2023;13(1):9412.

19. Abdalla S, Isaksen L, Janssen PAEM, Wedi N. Effective spectral resolution of ECMWF atmospheric forecast models. ECMWF Newsl. 2013;137:19–22.

20. Hansen SBK. Guidance on mesoscale wind mapping. Washington (DC): World Bank; 2018. Report No.: 132951.

21. Xie SP, et al. Predictive understanding of regional climate change. Nat Clim Change. 2015; 5:921–930.

22. Murphy J. Predictions of climate change over Europe using statistical and dynamic downscaling techniques. Int J Climatol. 2000; 20:489–501.

23. Slivinski LC, Compo GP, Whitaker JS, Sardeshmukh PD, Giese BS, McColl C, et

al. Towards a more reliable historical reanalysis: improvements for version 3 of the twentieth-century reanalysis system. Q J R Meteorol Soc. 2019;145(724):2876–2908.

24. Shiogama H, Abe M, Tatebe H. MIROC6 model output prepared for CMIP6 ScenarioMIP. Earth Syst Grid Fed. 2019. doi:10.22033/ESGF/CMIP6.898.

25. Hersbach H, Bell B, Berrisford P, Biavati G, Horányi A, Muñoz Sabater J, et al. ERA5 hourly data on single levels from 1940 to present. Copernicus Climate Change Service (C3S). 2023. doi:10.24381/cds.adbb2d47.

26. Smola AJ, Schölkopf B. Tutorial on support vector regression. Stat Comput. 2004; 14:199–222.

27. Al-Anazi AF, Gates ID. Support vector regression to predict porosity and permeability: effect of sample size. Comput Geosci. 2012; 39:64–76.

28. Cherkassky, V., & Ma, Y. Practical selection of SVM parameters and noise estimation for SVM regression. Neural Networks. 17(1): 113-126. (2004). https://doi.org/10.1016/S0893-6080(03)00169-2

29. Sivapragasam C, Liong SY, Pasha MFK. Rainfall and runoff forecasting with the SVM approach. J Hydroinform. 2001; 3(3):141–152. doi:10.2166/hydro.2001.0014.

30. Chen H, Chandrasekar V, Cifelli R, Xie P. Machine learning system for

precipitation estimation using satellite and ground radar network observations. IEEE Trans Geosci Remote Sens. 2019; 58(2):982–994.

31. Fan J, et al. Comparison of support vector machine and extreme gradient boosting for predicting daily global solar radiation. Energy Convers Manag. 2018; 164:102–111. doi:10.1016/j.enconman.2018.02.087.

32. Sachindra DA, Ahmed K, Rashid MM, Shahid S, Perera BJC. Statistical downscaling of precipitation using machine learning techniques. Atmos Res. 2018; 212:240–258. doi:10.1016/j.atmosres.2018.05.022.

33. Intel Corporation. Intel® Extension for Scikit-learn [Internet]. Available from: https://www.intel.com/content/www/us/en/developer/tools/oneapi/scikit-learn.html

34. Pedregosa F, Varoquaux G, Gramfort A, Michel V, Thirion B, Grisel O, et al. Scikit-learn: machine learning in Python. J Mach Learn Res. 2011; 12:2825–2830.

35. Smets K, Verdonk B, Jordaan EM. Evaluation of performance measures for SVR hyperparameter selection. In: Proc Int Joint Conf Neural Netw; 2007. p. 637–642. doi:10.1109/IJCNN.2007.4371031.

36. Yoshikane T, Yoshimura K. Bias correction method for precipitation by recognizing mesoscale precipitation systems corresponding to weather conditions.

PLoS Water. 2022;1(5):e0000016.

37. Vapnik V. The nature of statistical learning theory. New York: Springer; 1999.

38. Takano Y. Support vector machine and the kernel method. J Oper Res Soc Jpn. 2020;65:304–309.

39. Lanzante JR, Nath MJ, Whitlock CE, Dixon KW, Adams-Smith D. Evaluation and improvement of tail behavior in the cumulative distribution function transform downscaling method. Int J Climatol. 2019; 39:2449–2460.

40. Batuwita R, Palade V. Class imbalance learning methods for support vector machines. In: Imbalanced Learning: Foundations, Algorithms, and Applications. 2013. p. 83.

41. Vrac M, Michelangeli PA. CDFt: distribution-based climate model bias correction. R Package. 2015.

Supporting information captions

S1 Fig. Annual mean climate values in the first 30 years of temperature (TEMP2M), downward longwave radiation (DLWR), and specific humidity (SHUM) in 20CR. The first 30 years range from 1955 to 1984. 20CR, MLDS_20CR, and ERA5 are 20th century reanalysis data, values estimated using 20CR data, and ERA5 reanalysis data, respectively.

S2 Fig. The same figure as S1 Fig. except for downward shortwave radiation (DSWR), surface pressure (SP), near-surface wind at 10 m (zonal) (U10M), respectively.

S3 Fig. The same figure as S1 Fig. except for near-surface wind at 10 m (meridional) (V10M) and precipitation (PREC), respectively.

S4 Fig. The 99th percentile values of hourly downward longwave radiation DLWR), specific humidity (SHUM), and downward shortwave radiation (DSWR) in the first 30 years, and the climate different values between the first and last 30 years in ERA5 and MLDS_20CR. The left, center, and right figures show the 99th percentile values in ERA5, the 99th percentile values in MLDS_20CR, and a scatter diagram of the 99th percentile values in ERA5 and MLDS_20CR, with correlation coefficient values (R) and RMSEs.

S5 Fig. The same figure as S4 Fig. except for surface pressure (SP) and wind at 10 m (zonal and meridional) (U10M and V10M), respectively.

S6 Fig. Estimation of climate change characteristics using this method. Annual mean climate difference values between the first 30 years (past) and the last 30 years (present) of downward longwave radiation (DLWR), specific humidity (SHUM), and surface pressure (SP) in 20CR, MLDS_20CR, and ERA5, respectively. Shaded areas indicate significant increases with 95% confidence intervals using Welch's t-test.

S7 Fig. The same figure as S6 Fig. except for wind at 10 m (zonal and meridional) (U10M and V10M), respectively.

S8 Fig. Relationship between climate change simulated by the climate model and the values estimated by this method. Scatter diagrams of annual mean climate difference values between the first 30 years (past) and the last 30 years (present) of MLDS_20CR for ERA5. Temperature (TEMP2M), downward longwave radiation (DLWR), specific humidity (SHUM), downward shortwave radiation (DSWR), surface pressure (SP), near-surface winds (zonal) at 10 m (U10M), near-surface winds (meridional) at 10 m (V10M), and precipitation (PREC). The ERA5 and MLDS_20CR were upscaled to match the resolution of 20CR. The redder the color, the higher the distribution density.

S9 Fig. Annual mean climate values in the 30 years of temperature (TEMP2M), downward longwave radiation (DLWR), and specific humidity (SHUM) in MIROC from 1985 to 2014.

S10 Fig. The same figure as S9 Fig. except for downward shortwave radiation (DSWR), surface pressure (SP), and near-surface wind at 10 m (zonal) (U10M), respectively.

S11 Fig. The same figure as S9 Fig. except for near-surface wind at 10 m (meridional) (V10M) and precipitation (PREC), respectively.

S12 Fig. Estimation of future climate change characteristics using CMIP6-MIROC data. Annual mean climate difference between the present 30 years (historical; 1985 to 2014) and future 30 years (SSP126; 2071–2100) of downward longwave radiation (DLWR), specific humidity (SHUM), and surface pressure (SP) in MIROC and MLDS_MIROC. Shaded areas indicate significant increases with 95% confidence intervals using Welch's t-test. Scatter diagrams of MIROC and MLDS_MIROC with correlation coefficient values (R) and RMSEs are shown on the right side of the figure.

S13 Fig. The same figure as S12 Fig. except for wind at 10 m (zonal and meridional) (U10M and V10M), respectively.

S14 Fig. Comparison with quantile mapping method. Time series of each variable at a specific grid point (130°E, 33°N) in July 1985. The blue, gray, orange, and red lines represent MLDS_20CR, ERA5, 20CR, and quantile mapping (QM), respectively.

S1 Table. Hyperparameters used in SVR (gamma, C, epsilon) and scale factors for each variable.

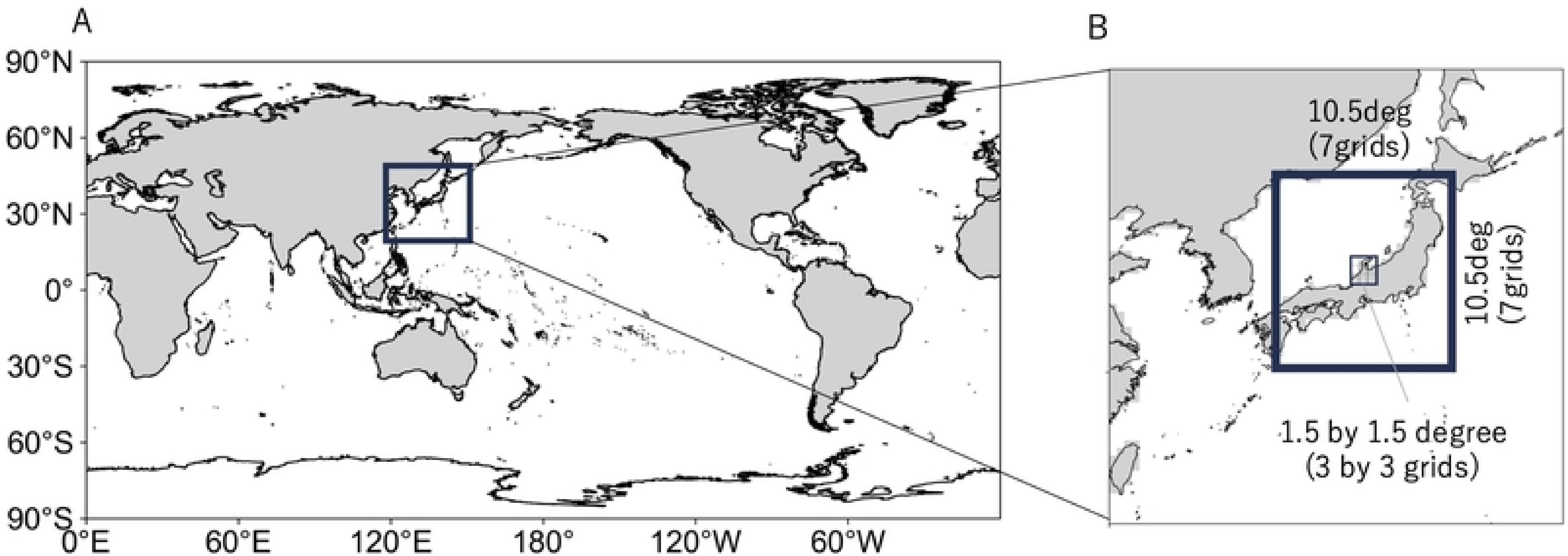
A
B
90°N
60°N
30°N
0°
30°S
60°S
90°S
0°E
60°E
120°E
180°
120°W
60°W
10.5deg
(7grids)
10.5deg
(7grids)
1.5 by 1.5 degree
(3 by 3 grids)

Fig1

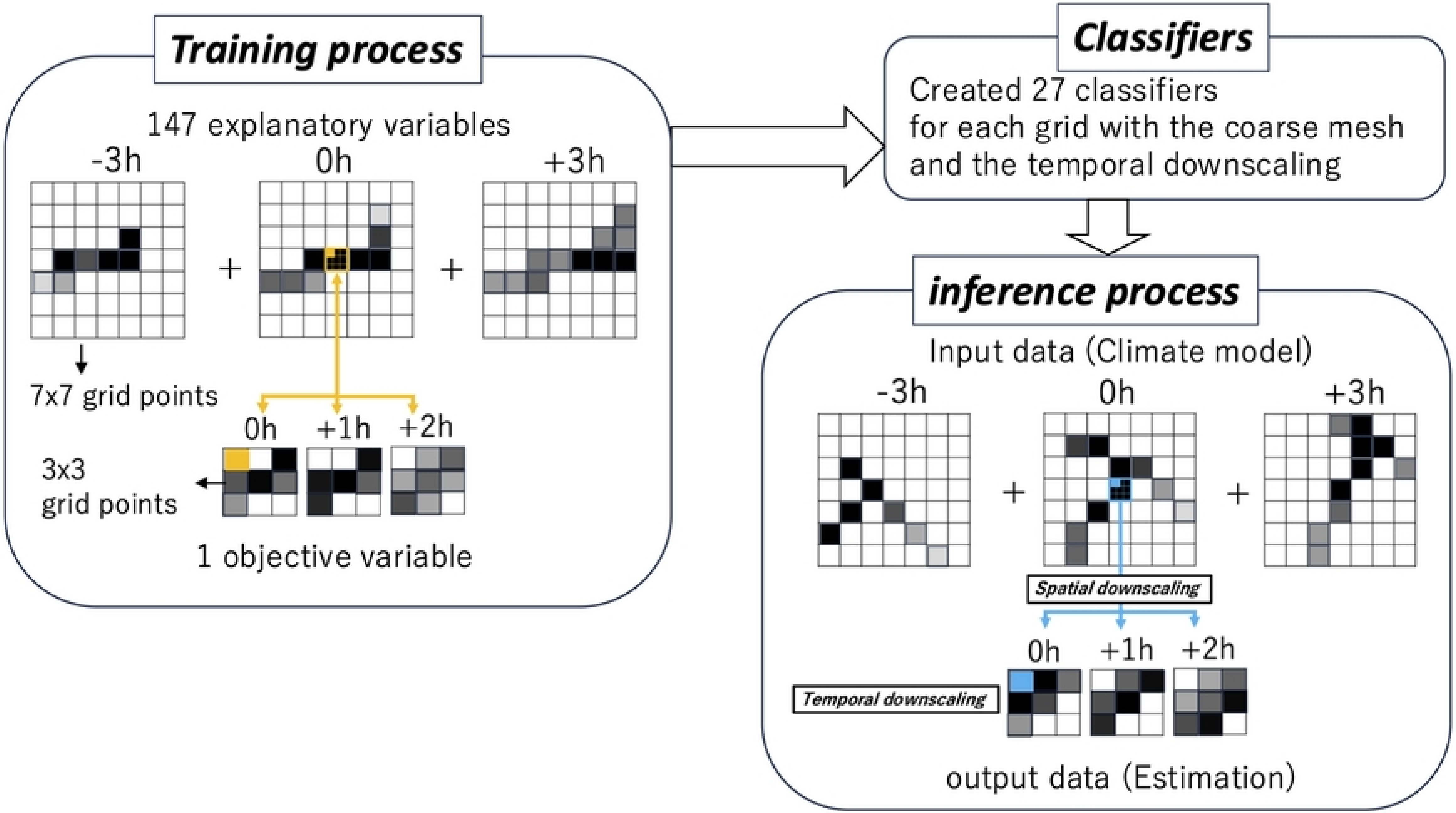
Training process
147 explanatory variables
-3h
0h
+3h
+
+
7x7 grid points
0h
+1h
+2h
3x3
grid points
1 objective variable
Classifiers
Created 27 classifiers
for each grid with the coarse mesh
and the temporal downscaling
inference process
Input data (Climate model)
-3h
0h
+3h
+
+
Spatial downscaling
0h
+1h
+2h
Temporal downscaling
output data (Estimation)

Fig2

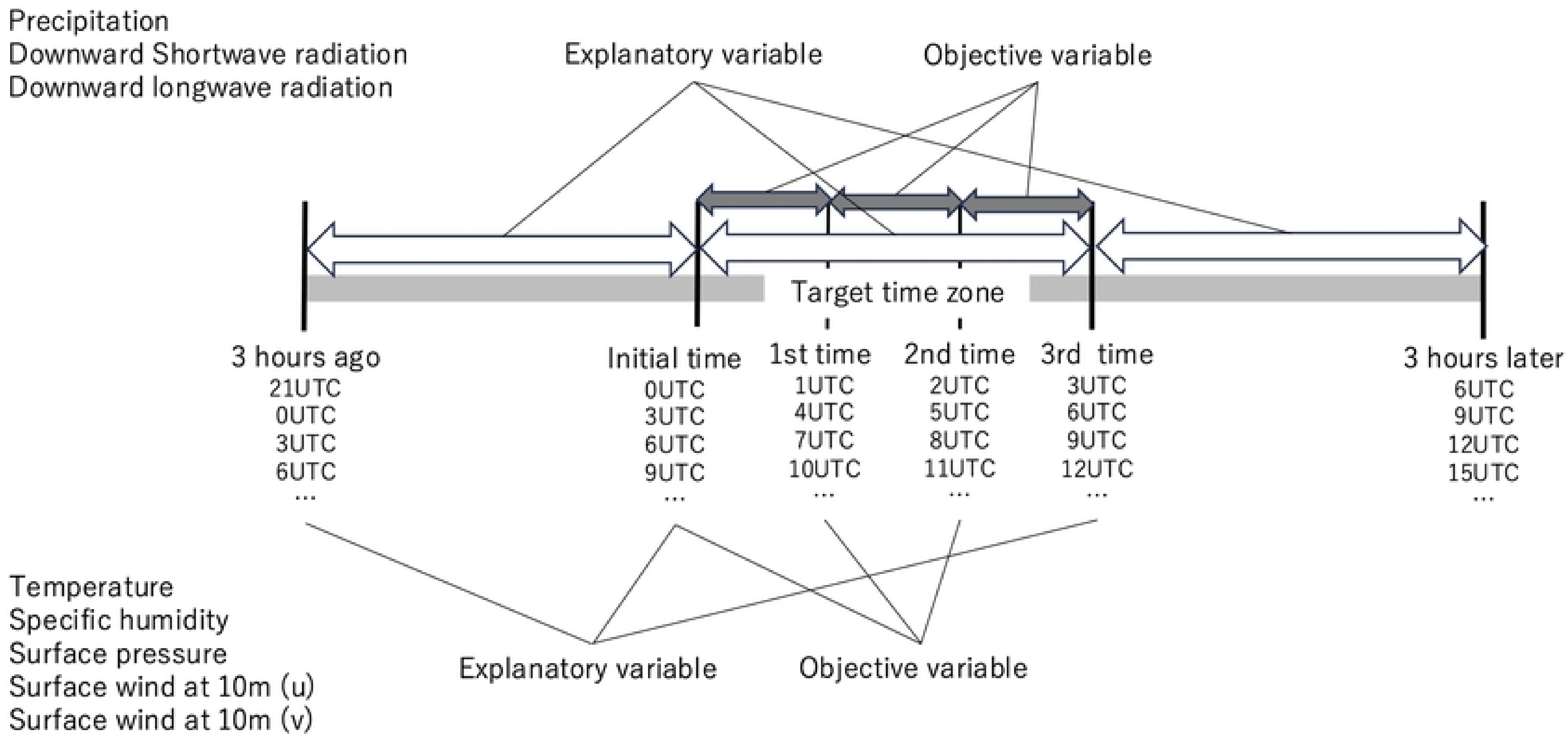
Precipitation
Downward Shortwave radiation
Downward longwave radiation
Explanatory variable
Objective variable
Target time zone
3 hours ago
21UTC
0UTC
3UTC
6UTC
...
Initial time
0UTC
3UTC
6UTC
9UTC
...
1st time
1UTC
4UTC
7UTC
10UTC
...
2nd time
2UTC
5UTC
8UTC
11UTC
...
3rd time
3UTC
6UTC
9UTC
12UTC
...
3 hours later
6UTC
9UTC
12UTC
15UTC
...
Temperature
Specific humidity
Surface pressure
Surface wind at 10m (u)
Surface wind at 10m (v)
Explanatory variable
Objective variable

Fig3

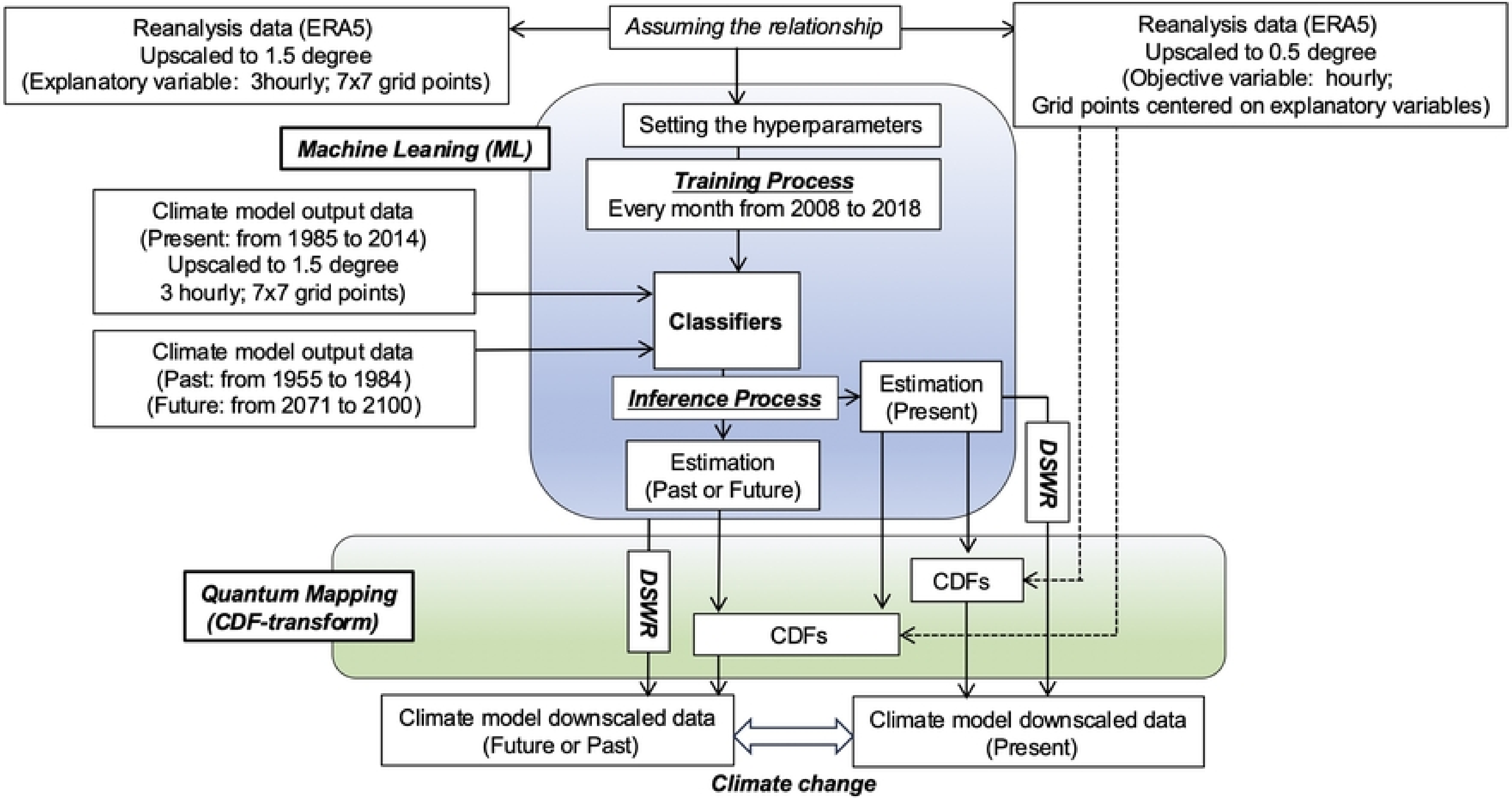
Reanalysis data (ERA5)
Upscaled to 1.5 degree
(Explanatory variable: 3hourly; 7x7 grid points)
Assuming the relationship
Reanalysis data (ERA5)
Upscaled to 0.5 degree
(Objective variable: hourly;
Grid points centered on explanatory variables)
Setting the hyperparameters
Machine Leaning (ML)
Training Process
Every month from 2008 to 2018
Climate model output data
(Present: from 1985 to 2014)
Upscaled to 1.5 degree
3 hourly; 7x7 grid points)
Classifiers
Climate model output data
(Past: from 1955 to 1984)
(Future: from 2071 to 2100)
Inference Process
Estimation
(Present)
DSWR
Estimation
(Past or Future)
CDFs
Quantum Mapping
(CDF-transform)
DSWR
CDFs
Climate model downscaled data
(Future or Past)
Climate model downscaled data
(Present)
Climate change

Fig4

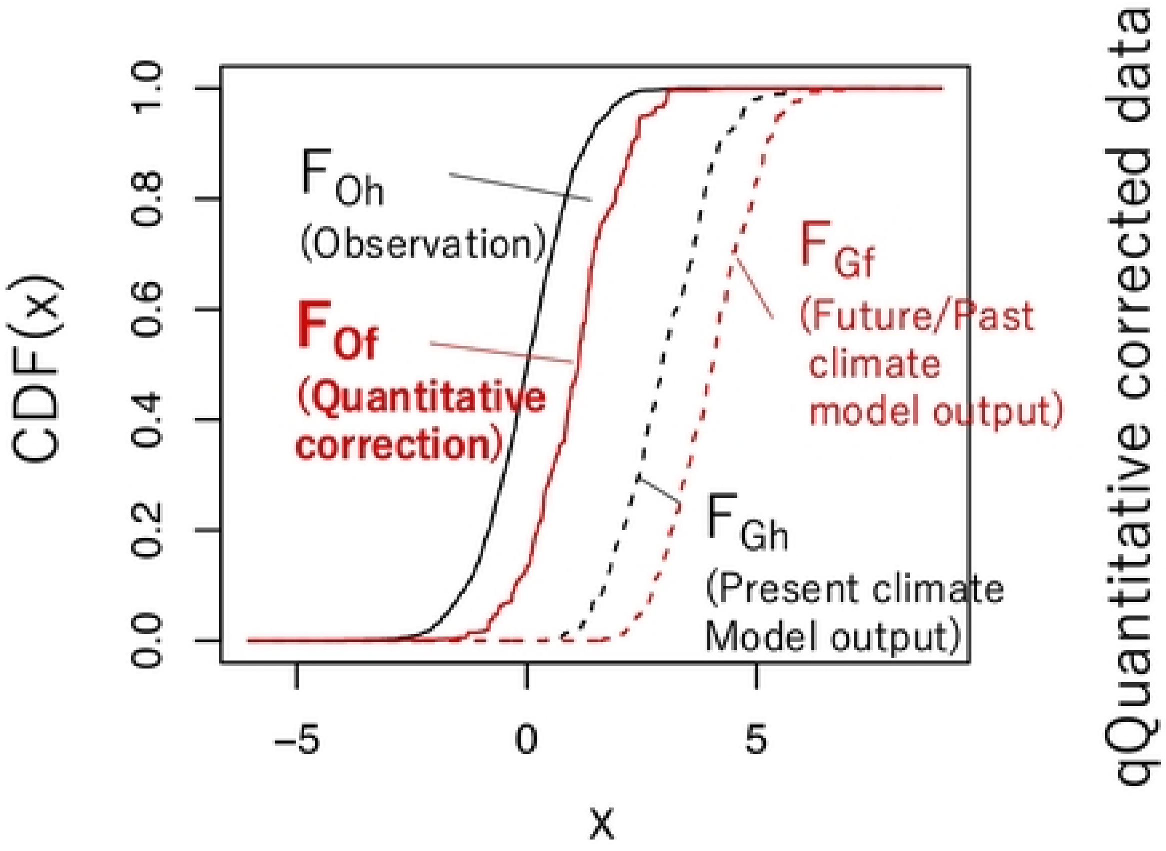

CDF(x)
x
F_{Oh}
(Observation)
F_{Of}
(Quantitative correction)
F_{Gf}
(Future/Past climate model output)
F_{Gh}
(Present climate Model output)
qQuantitative corrected data
Climate model data

Fig5

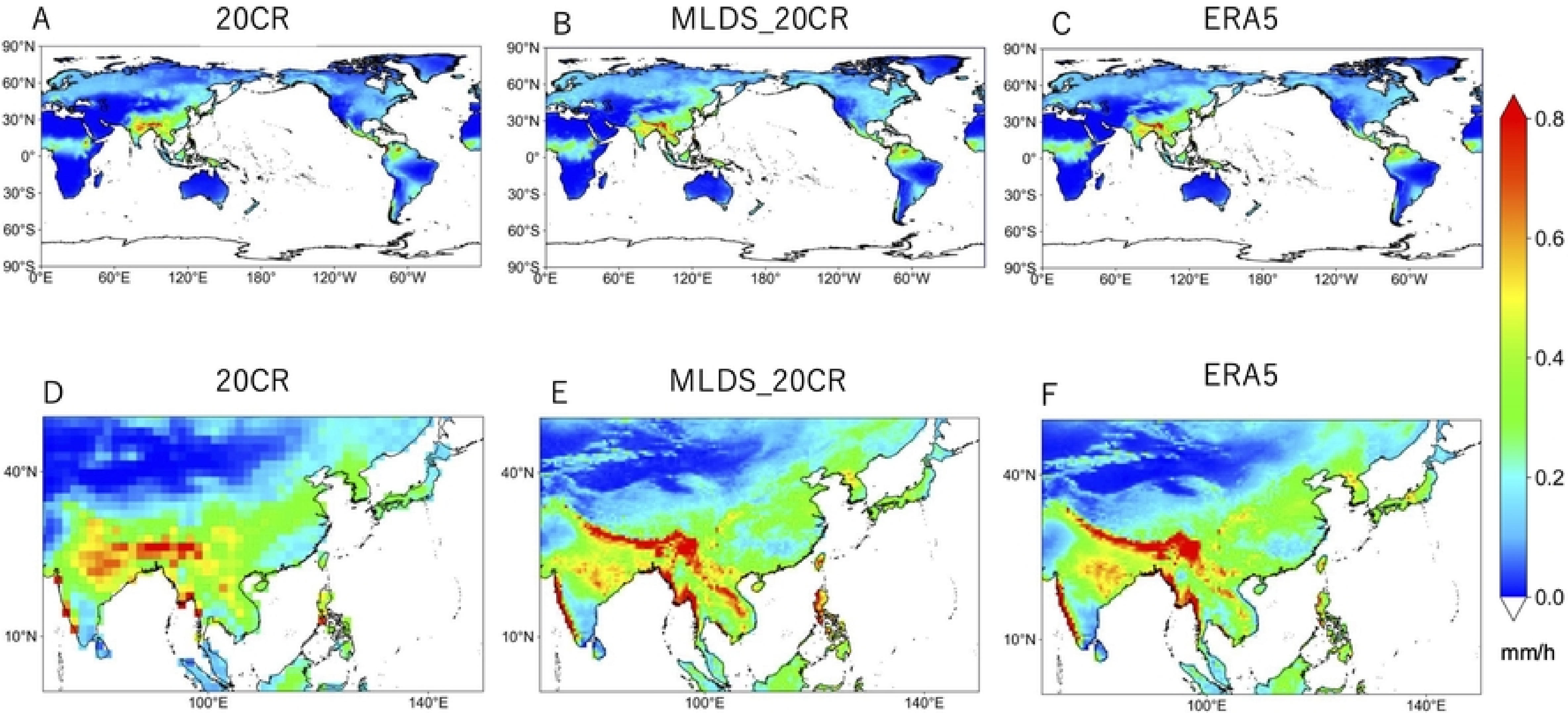
A
20CR
B
MLDS_20CR
C
ERA5
90°N
60°N
30°N
0°
30°S
60°S
90°S
0°E
60°E
120°E
180°
120°W
60°W
D
20CR
E
MLDS_20CR
F
ERA5
40°N
10°N
100°E
140°E
0.8
0.6
0.4
0.2
0.0
mm/h

Fig6

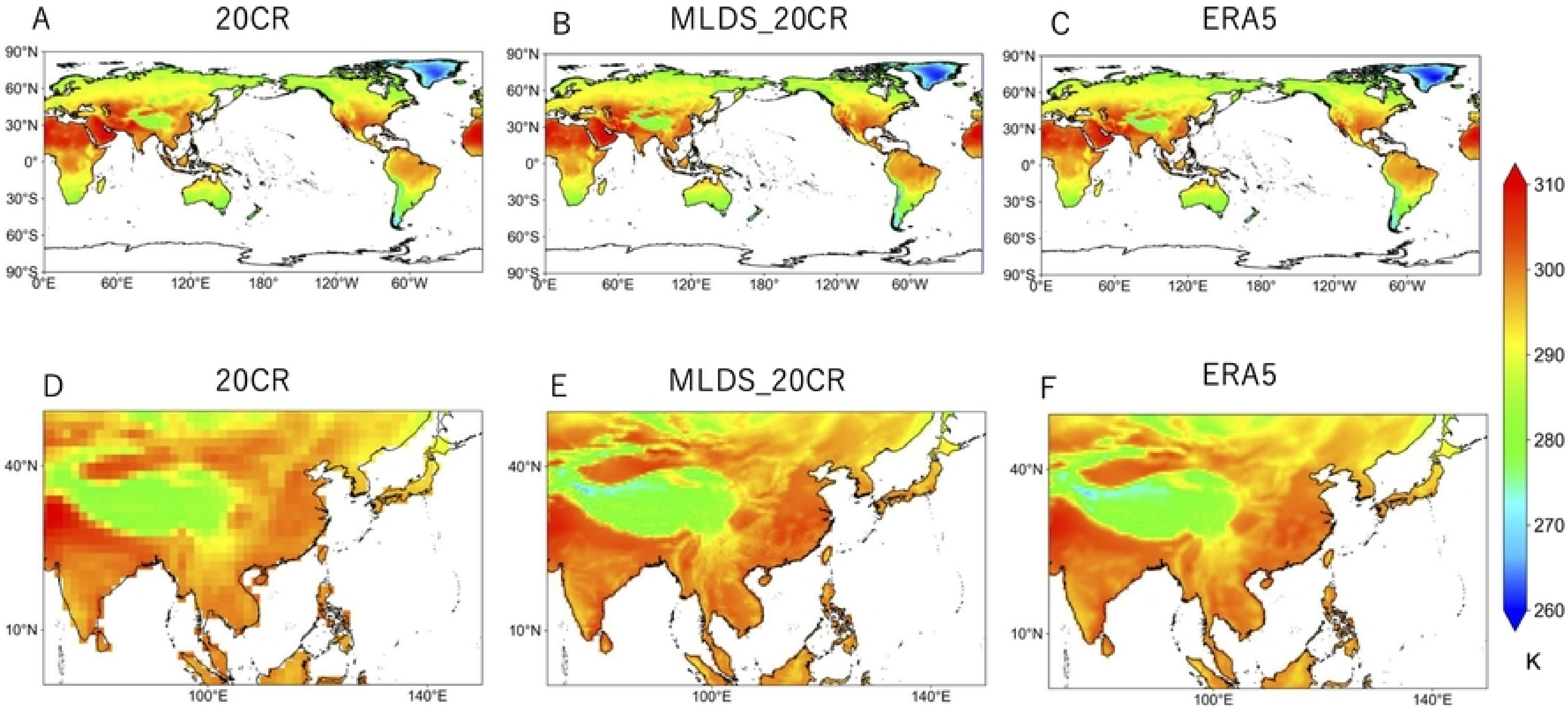
A
20CR
B
MLDS_20CR
C
ERA5
D
20CR
E
MLDS_20CR
F
ERA5
90°N
60°N
30°N
0°
30°S
60°S
90°S
0°E
60°E
120°E
180°
120°W
60°W
40°N
10°N
100°E
140°E
310
300
290
280
270
260
K

Fig7

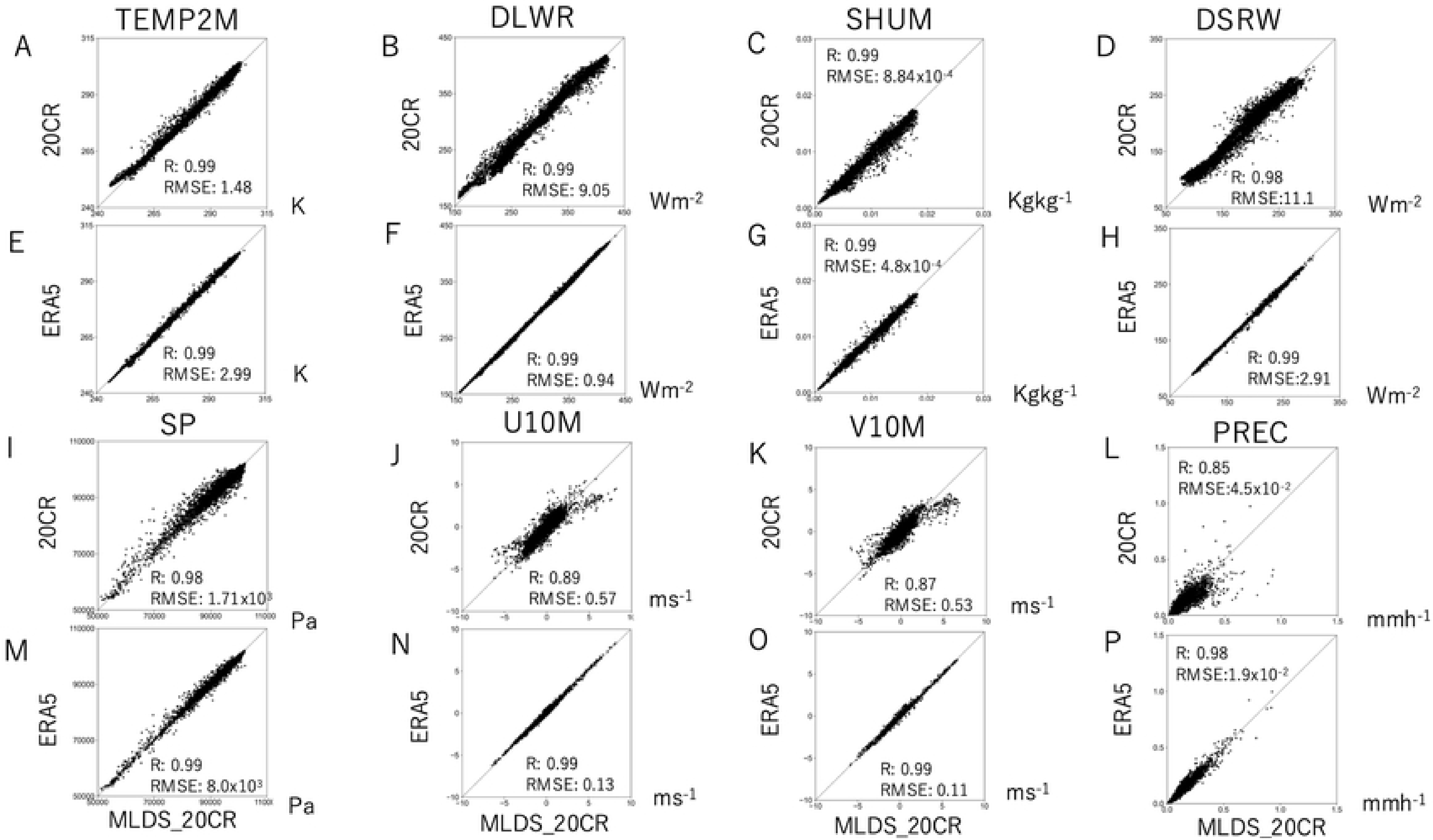

TEMP2M
DLWR
SHUM
DSRW
A
B
C
D
20CR
R: 0.99
RMSE: 1.48
K
R: 0.99
RMSE: 9.05
Wm-2
R: 0.99
RMSE: 8.84x10-4
Kgkg-1
R: 0.98
RMSE:11.1
Wm-2
E
F
G
H
ERA5
R: 0.99
RMSE: 2.99
K
R: 0.99
RMSE: 0.94
Wm-2
R: 0.99
RMSE: 4.8x10-4
Kgkg-1
R: 0.99
RMSE:2.91
Wm-2
SP
U10M
V10M
PREC
I
J
K
L
R: 0.98
RMSE: 1.71x103
Pa
R: 0.89
RMSE: 0.57
ms-1
R: 0.87
RMSE: 0.53
ms-1
R: 0.85
RMSE:4.5x10-2
mmh-1
M
N
O
P
R: 0.99
RMSE: 8.0x103
Pa
R: 0.99
RMSE: 0.13
ms-1
R: 0.99
RMSE: 0.11
ms-1
R: 0.98
RMSE:1.9x10-2
mmh-1
MLDS_20CR

Fig8

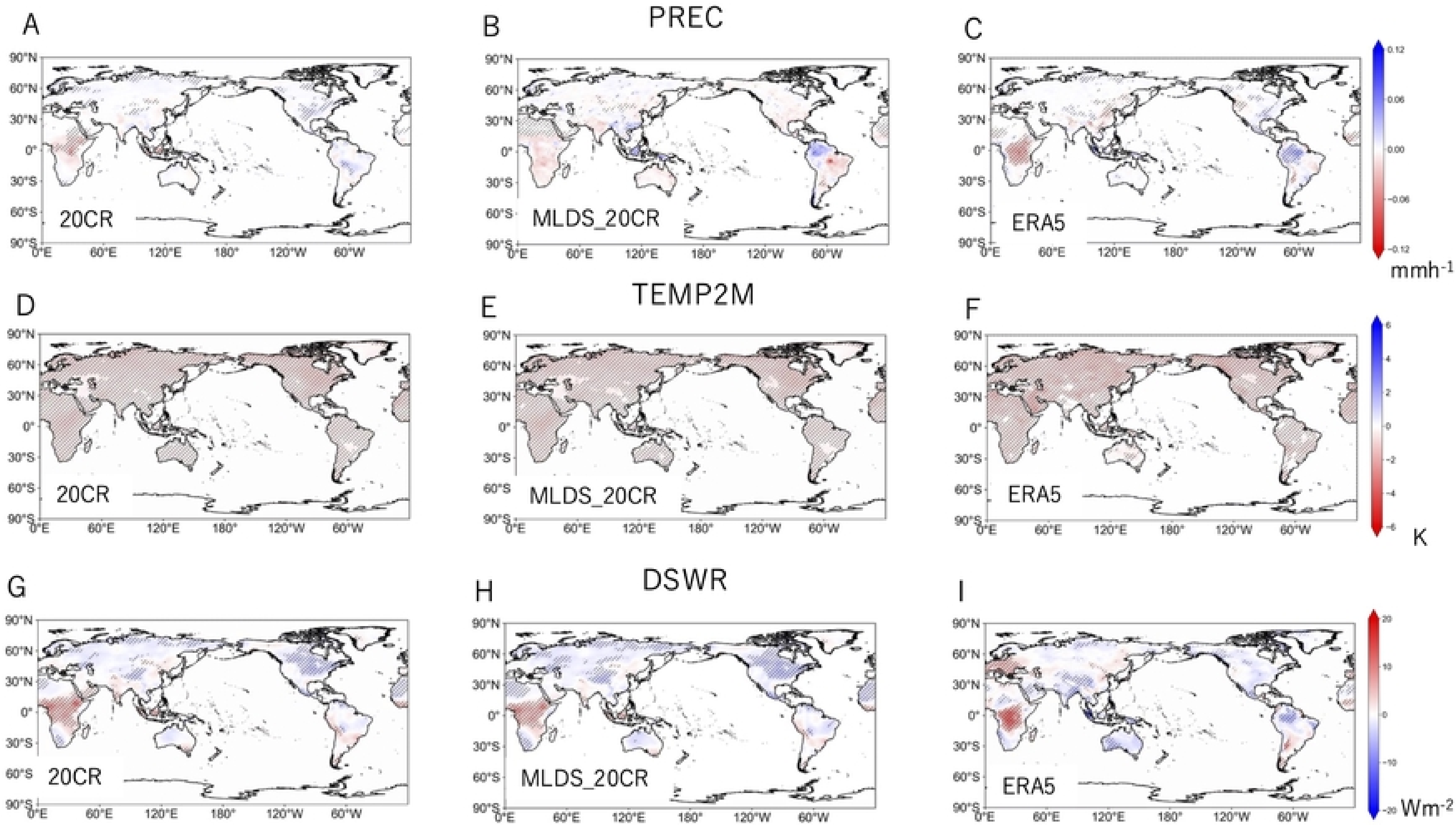
PREC
TEMP2M
DSWR
A
B
C
D
E
F
G
H
I
20CR
MLDS_20CR
ERA5
mmh-1
K
Wm-2
90°N
60°N
30°N
0°
30°S
60°S
90°S
0°E
60°E
120°E
180°
120°W
60°W

Fig9

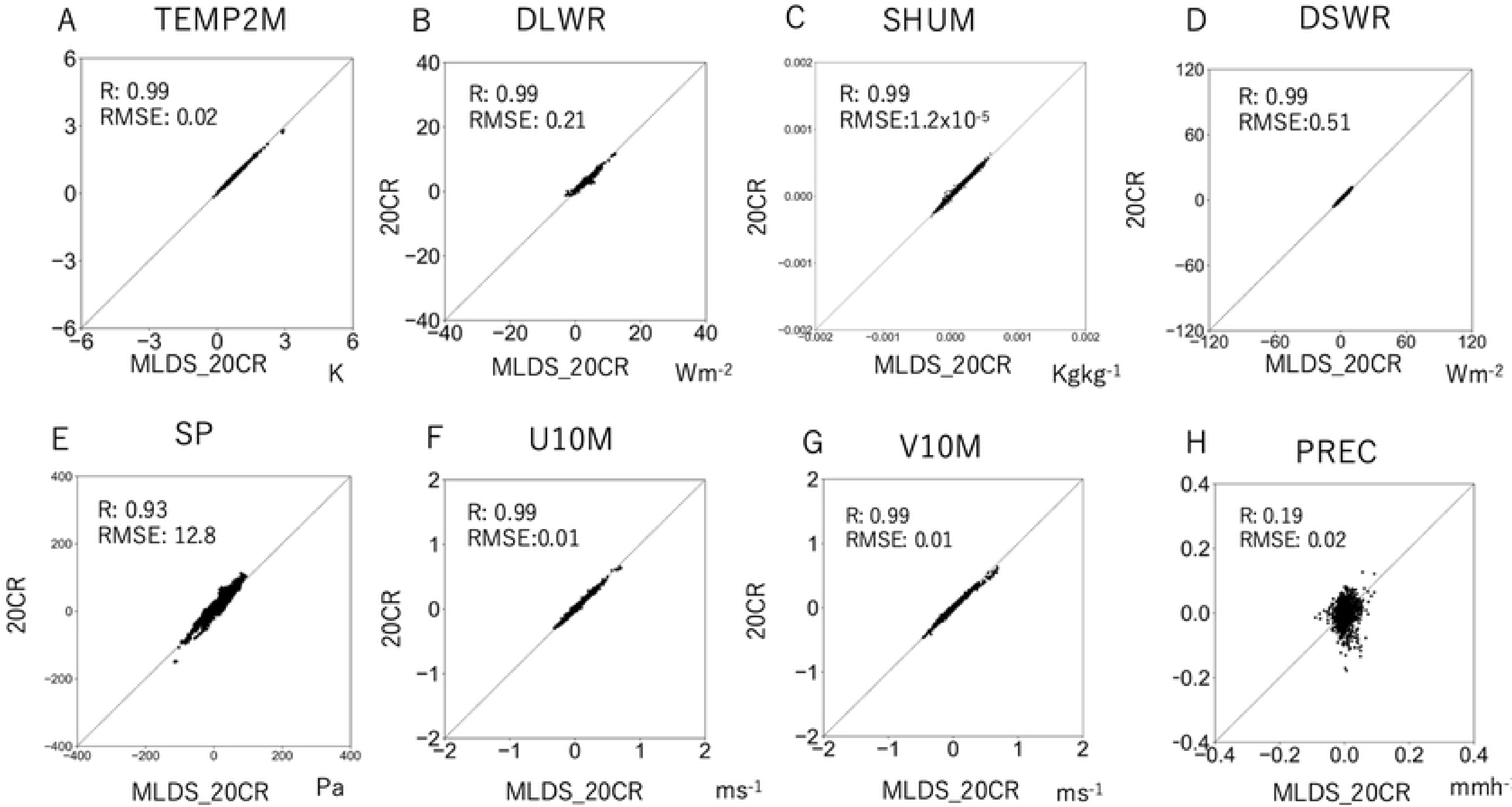

A TEMP2M
R: 0.99
RMSE: 0.02
MLDS_20CR
K
B DLWR
R: 0.99
RMSE: 0.21
20CR
MLDS_20CR
Wm-2
C SHUM
R: 0.99
RMSE:1.2x10-5
20CR
MLDS_20CR
Kgkg-1
D DSWR
R: 0.99
RMSE:0.51
20CR
MLDS_20CR
Wm-2
E SP
R: 0.93
RMSE: 12.8
20CR
MLDS_20CR
Pa
F U10M
R: 0.99
RMSE:0.01
20CR
MLDS_20CR
ms-1
G V10M
R: 0.99
RMSE: 0.01
20CR
MLDS_20CR
ms-1
H PREC
R: 0.19
RMSE: 0.02
MLDS_20CR
mmh-1

Fig10

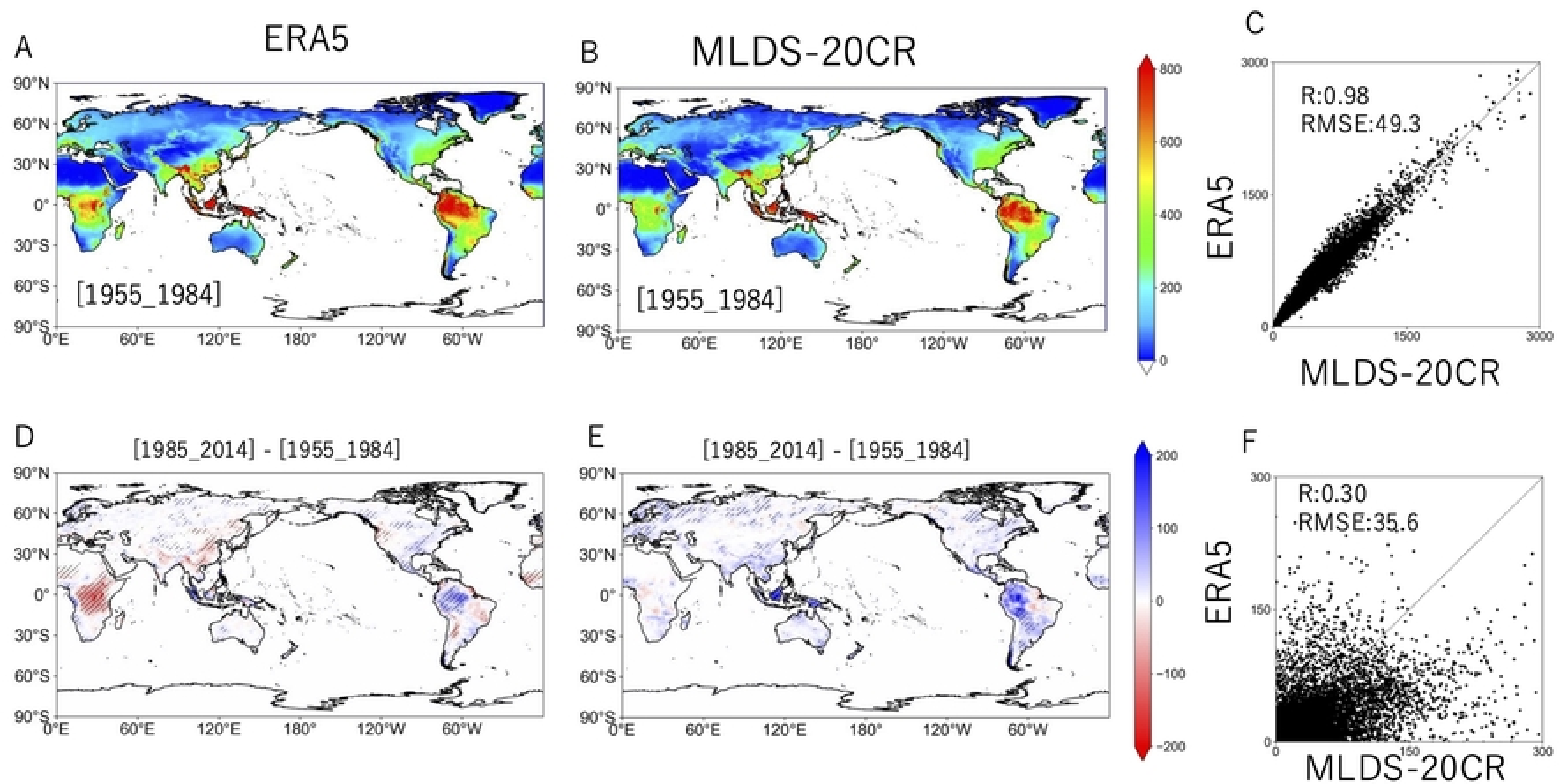
A
ERA5
B
MLDS-20CR
C
R:0.98
RMSE:49.3
ERA5
MLDS-20CR
[1955_1984]
[1955_1984]
D
[1985_2014] - [1955_1984]
E
[1985_2014] - [1955_1984]
F
R:0.30
RMSE:35.6
ERA5
MLDS-20CR
90°N
60°N
30°N
0°
30°S
60°S
90°S
0°E
60°E
120°E
180°
120°W
60°W
800
600
400
200
0
200
100
0
-100
-200
3000
1500
0
300
150

Fig11

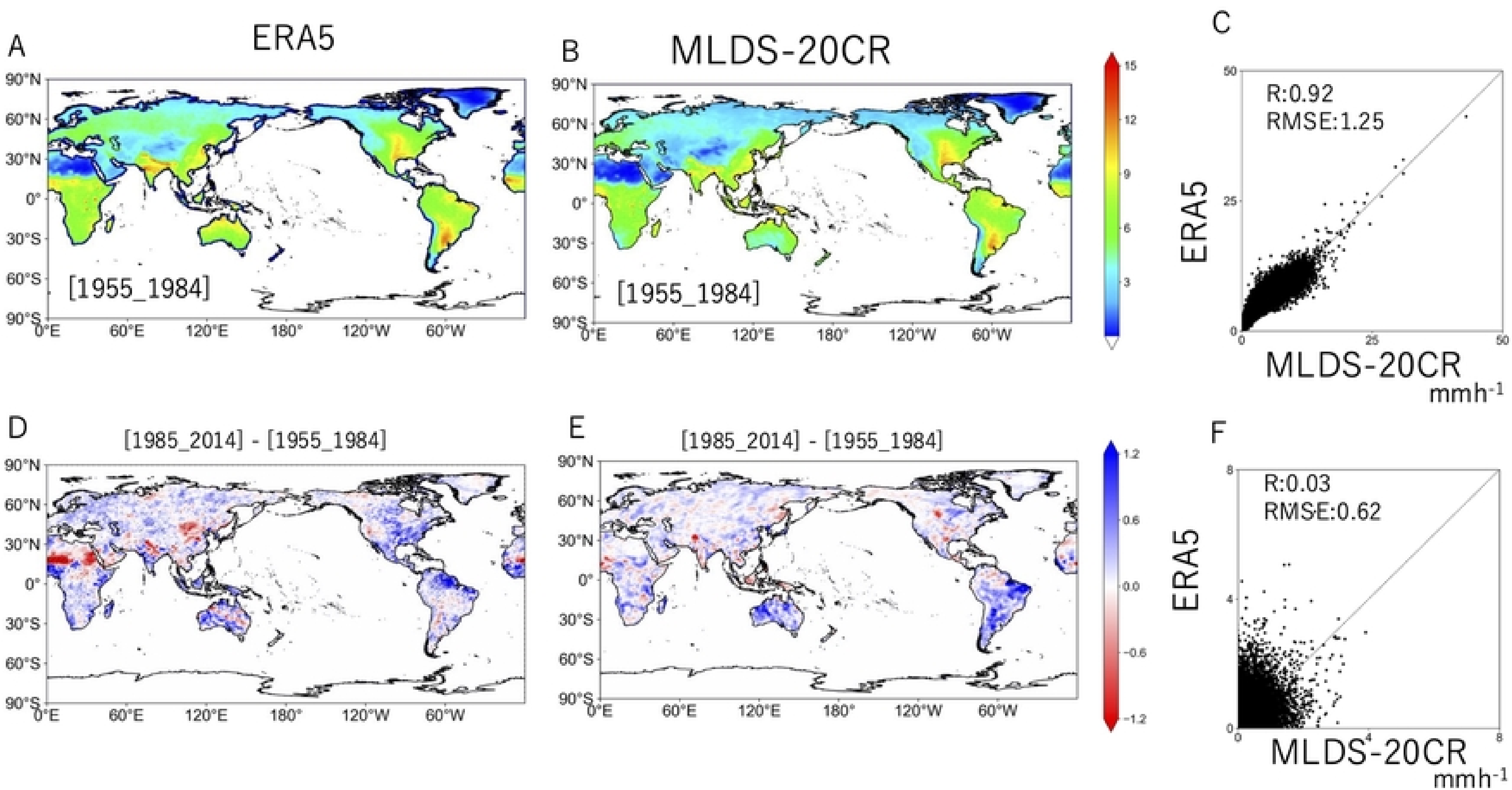
A
ERA5
B
MLDS-20CR
C
R:0.92
RMSE:1.25
ERA5
MLDS-20CR
mmh-1
[1955_1984]
[1955_1984]
D
[1985_2014] - [1955_1984]
E
[1985_2014] - [1955_1984]
F
R:0.03
RMSE:0.62
ERA5
MLDS-20CR
mmh-1
90°N
60°N
30°N
0°
30°S
60°S
90°S
0°E
60°E
120°E
180°
120°W
60°W

Fig12

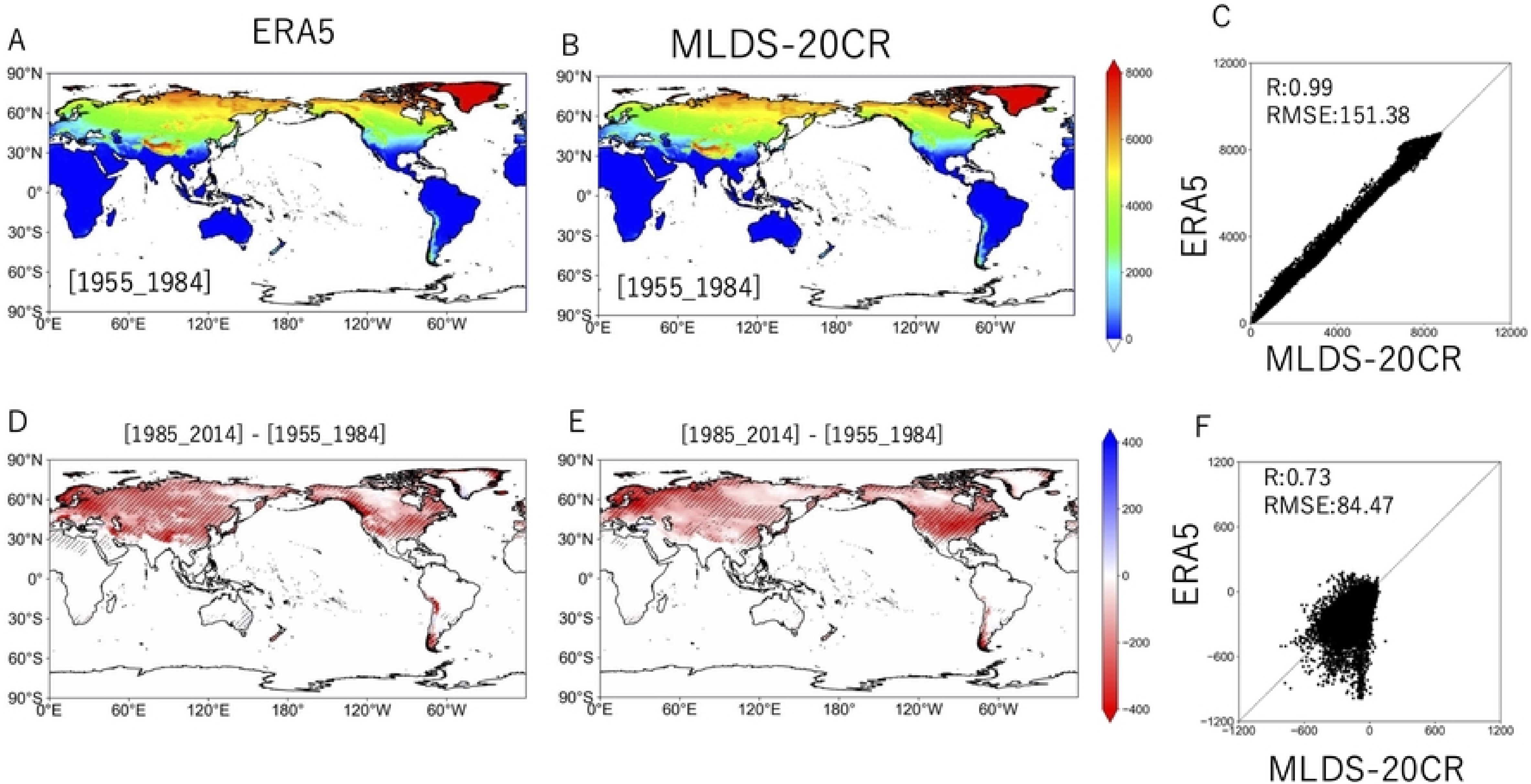
A
ERA5
[1955_1984]
B
MLDS-20CR
[1955_1984]
C
R:0.99
RMSE:151.38
ERA5
MLDS-20CR
D
[1985_2014] - [1955_1984]
E
[1985_2014] - [1955_1984]
F
R:0.73
RMSE:84.47
ERA5
MLDS-20CR

Fig13

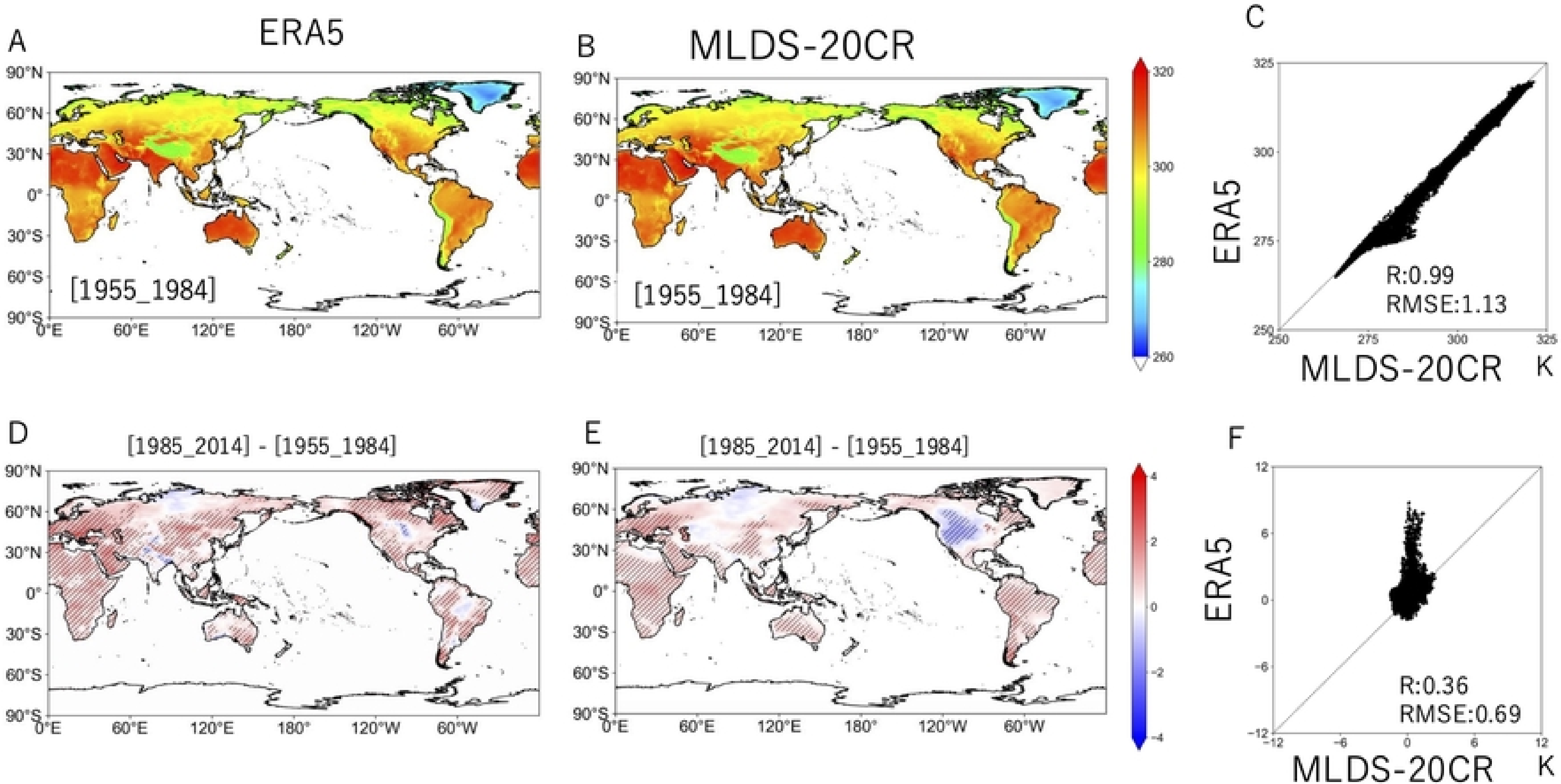

A
ERA5
B
MLDS-20CR
C
[1955_1984]
[1955_1984]
R:0.99
RMSE:1.13
ERA5
MLDS-20CR
K
D
[1985_2014] - [1955_1984]
E
[1985_2014] - [1955_1984]
F
R:0.36
RMSE:0.69
ERA5
MLDS-20CR
K

Fig14

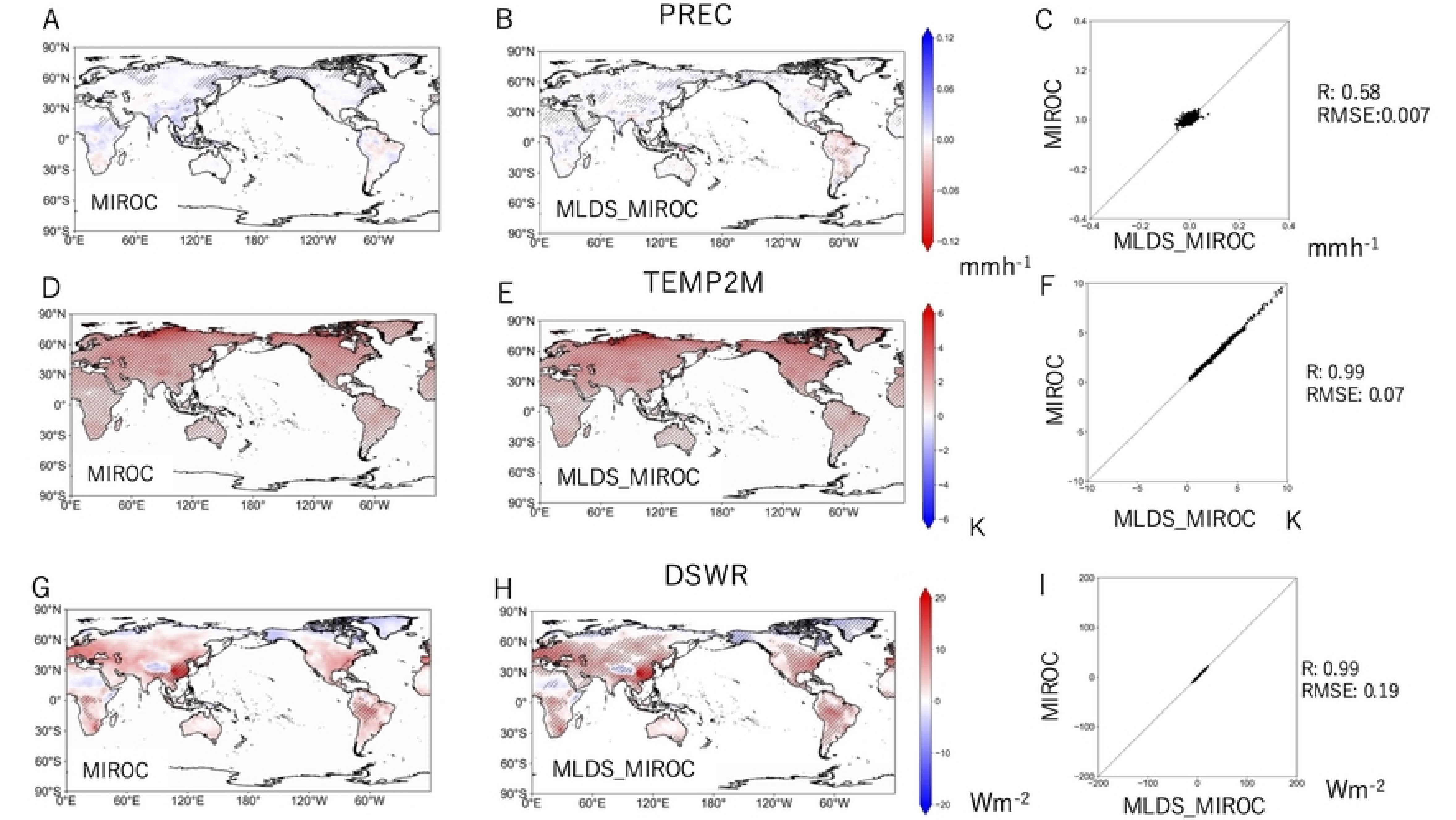

PREC
TEMP2M
DSWR
MIROC
MLDS_MIROC
R: 0.58
RMSE:0.007
mmh-1
R: 0.99
RMSE: 0.07
K
R: 0.99
RMSE: 0.19
Wm-2

Fig15

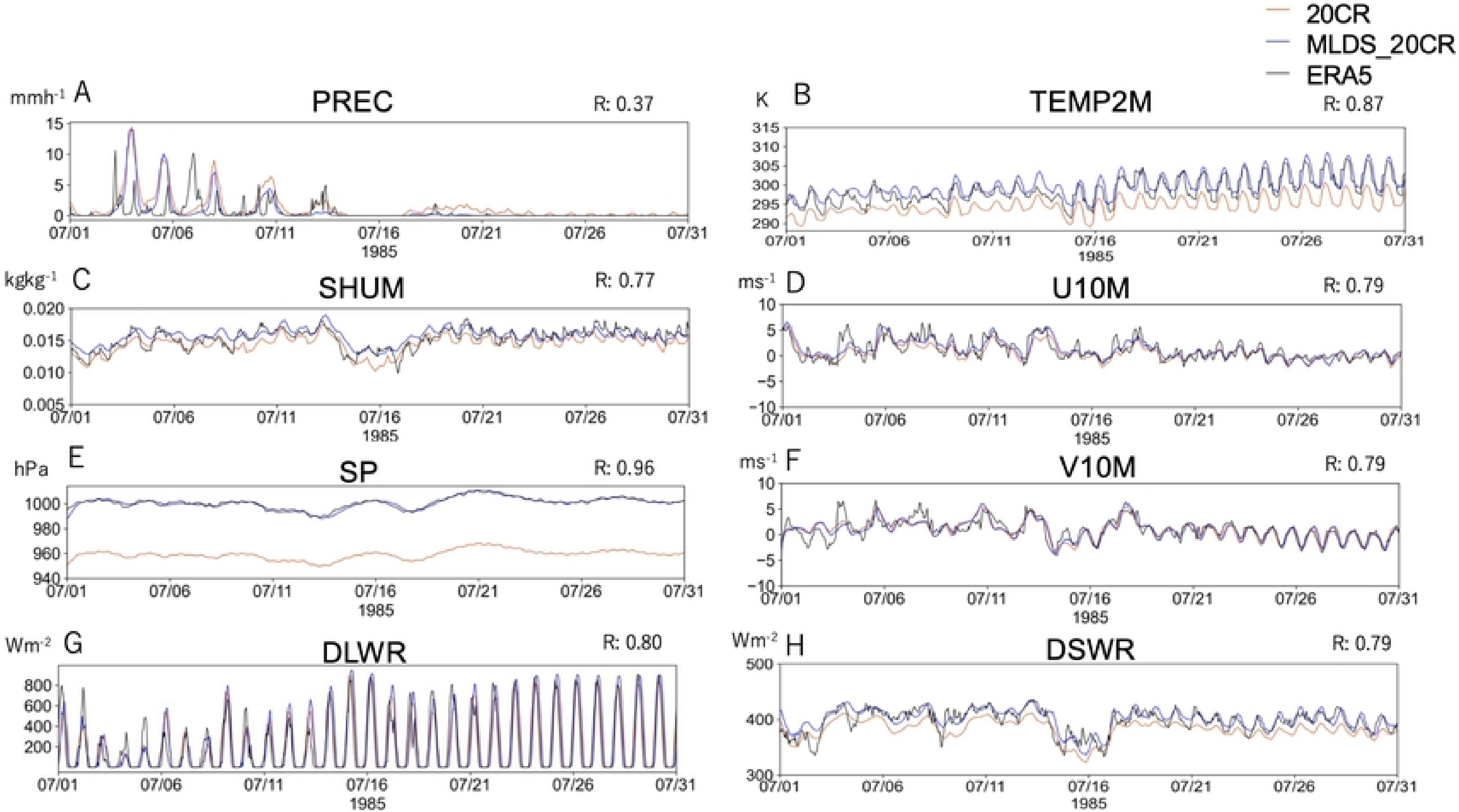

20CR
MLDS_20CR
ERA5
mmh-1 A
PREC
R: 0.37
K B
TEMP2M
R: 0.87
kgkg-1 C
SHUM
R: 0.77
ms-1 D
U10M
R: 0.79
hPa E
SP
R: 0.96
ms-1 F
V10M
R: 0.79
Wm-2 G
DLWR
R: 0.80
Wm-2 H
DSWR
R: 0.79
07/01
07/06
07/11
07/16
07/21
07/26
07/31
1985

Fig16